

Rotating neutron star models with magnetic field

M. Bocquet^{1,2}, S. Bonazzola¹, E. Gourgoulhon^{1,*}, and J. Novak^{1,2}

¹ Département d'Astrophysique Relativiste et de Cosmologie (UPR 176 C.N.R.S.), Observatoire de Paris, Section de Meudon, F-92195 Meudon Cedex, France

e-mail : gourgoulhon@obspm.fr

² Ecole Polytechnique, F-91128 Palaiseau Cedex, France

Received date; accepted date

Abstract. We present the first numerical solutions of the coupled Einstein-Maxwell equations describing rapidly rotating neutron stars endowed with a magnetic field. These solutions are fully relativistic and self-consistent, all the effects of the electromagnetic field on the star's equilibrium (Lorentz force, spacetime curvature generated by the electromagnetic stress-energy) being taken into account. The magnetic field is axisymmetric and poloidal. Five dense matter equations of state are employed. The partial differential equation system is integrated by means of a pseudo-spectral method. Various tests passed by the numerical code are presented. The effects of the magnetic field on neutron stars structure are then investigated, especially by comparing magnetized and non-magnetized configurations with the same baryon number. The deformation of the star induced by the magnetic field is important only for huge values of B ($B > 10^{10}$ T). The maximum mass as well as the maximum rotational velocity are found to increase with the magnetic field. The maximum allowable poloidal magnetic field is of the order of 10^{14} T and is reached when the magnetic pressure is comparable to the fluid pressure at the centre of the star. For such values, the maximum mass of neutron stars is found to increase by 13 to 29% (depending upon the EOS) with respect to the maximum mass of non-magnetized stars.

Key words: relativity – stars: magnetic fields – stars: neutron – stars: rotating – pulsars: general – methods: numerical

spin slowdown of pulsars via the magnetic dipole braking model; for the 558 pulsars of the catalog by Taylor et al. (1993), it ranges from $B = 1.7 \cdot 10^{-5}$ GT¹ (PSR B1957+20) up to $B = 2.1$ GT (PSR B0154+61), with a median value $B = 0.13$ GT, most of young pulsars having a surface field in the range $B \sim 0.1 - 2$ GT. From the theoretical point of view, a considerable amount of studies have been devoted to the structure of the magnetic field *outside* the neutron star, in the so-called *magnetosphere*, in relation with the pulsar emission mechanism (for a review, see e.g. Michel 1991). The studies of the magnetic field *inside* neutron stars are far less abundant. Only recently, some works have been devoted to the origin and the evolution of the internal magnetic field, all of them in the non-relativistic approximation (Thompson & Duncan 1993, Urpin & Ray 1994, Wiebicke & Geppert 1995, Urpin & Shalybkov 1995).

Beside these studies of neutron star magnetic field, there exists a growing number of numerical computations of rapidly rotating neutron stars in the full framework of general relativity, taking into account the most sophisticated equations of state of dense matter to date (cf. Salgado et al. 1994a,b and reference therein, as well as Cook et al. 1994b, Eriguchi et al. 1994, Friedman & Ipser 1992). But in all these models the magnetic field is ignored. The present work is the first attempt to compute numerical models of rotating neutron stars with magnetic field in a self-consistent way, by solving the Einstein-Maxwell equations describing stationary axisymmetric rotating objects with internal electric currents. In this way, the models presented below

1. are fully relativistic, i.e. all the effects of general relativity are taken into account, on the gravitational field as well as on the electromagnetic field.

1. Introduction

Neutron stars are known to possess strong magnetic fields. Their polar field strength is deduced from the observed

Send offprint requests to: E. Gourgoulhon

* author to whom the proofs should be sent

¹ In this article, we systematically use S.I. units, so that the magnetic field amplitude is measured in teslas (T) or, more conveniently in gigateslas ($1 \text{ GT} = 10^9 \text{ T}$). We recall that $1 \text{ GT} = 10^{13}$ gauss.

2. are self-consistent, i.e. the electromagnetic field is generated by some electric current distribution and the equilibrium of the matter is given by the balance between the gravitational force, the pressure gradient and the Lorentz force corresponding to the electric current. Moreover, the electromagnetic energy density is taken into account in the source of the gravitational field.
3. give the solution in all space, from the star's centre to infinity, without any approximation on the boundary conditions.
4. use various equations of state proposed in the literature for describing neutron star matter.

The restrictions of our models are the following ones:

1. We consider strictly stationary configurations. This excludes magnetic dipole moment non-aligned with the rotation axis. Indeed, in the non-aligned case, the star radiates away electromagnetic waves as well as gravitational waves (due to the deviation from axisymmetry induced by a magnetic axis different from the rotation axis); hence it loses energy and angular momentum, so that this situation does not correspond to any stationary solution of Einstein equation. Thus the stationary hypothesis implies that we restrict ourselves to axisymmetric configurations, with the magnetic axis aligned with the rotation axis.
2. Moreover, we consider only *poloidal* magnetic fields (i.e. \mathbf{B} lying in the meridional planes). Indeed, if the magnetic field had, in addition to the poloidal part, a *toroidal* component (i.e. a component perpendicular to the meridional planes), the *circularity* property of spacetime would be broken, which means that the two Killing vectors associated with the stationarity and the axisymmetry would no longer be orthogonal to a family of 2-surfaces (cf. Carter 1973, p. 159). In the circular case, a coordinate system (t, r, θ, ϕ) can be found such that the components of the metric tensor \mathbf{g} are zero except for the diagonal terms and only one off-diagonal term ($g_{t\phi}$). In the non-circular case, only one component of \mathbf{g} can be set to zero ($g_{r\theta}$), resulting in much more complicated gravitational field equations (Gourgoulhon & Bonazzola 1993). On the contrary, perfect fluid stars with purely rotational motion (no convection) generate circular spacetimes and poloidal magnetic fields preserve this property (Carter 1973).
3. Being not interested in modelling pulsar magnetospheres, we suppose that the neutron star is surrounded by vacuum².

The numerical code we use is an electromagnetic extension of the code presented in Bonazzola et al. 1993 (hereafter BGS_M), which was devoted to perfect fluid rotating stars and used to compute neutron star models with

² by *vacuum* we mean that there is no matter outside the star; nevertheless there is some electromagnetic field, so that the total stress-energy tensor (right-hand side of the Einstein equation) is not zero outside the star (*electrovac* spacetime).

various equations of state of dense matter (Salgado et al. 1994a,b). We will not give here the complete list of the equations to be solved but only the electromagnetic ones (Maxwell equations) in Sect. 2, referring to BGS_M for the gravitational part. Likewise we will not present the numerical technique, based on a pseudo-spectral method, since it has been detailed in BGS_M. We will discuss in Sect. 3 only the numerical procedure and tests of the electromagnetic part of the code. We analyze the effects of the magnetic field on static configurations in Sect. 4 and on rotating configurations in Sect. 5, the Sect. 6 describing in detail the case of constant baryon number sequences. Finally Sect. 7 summarizes the main conclusions of this study.

2. Electromagnetic equations

2.1. Definitions and notations

Following BGS_M, we use MSQI (*Maximal Slicing - Quasi-Isotropic*) coordinates (t, r, θ, ϕ) , in which the metric tensor \mathbf{g} takes the form

$$g_{\alpha\beta} dx^\alpha dx^\beta = -N^2 dt^2 + A^4 \left[B^2 r^2 \sin^2 \theta (d\phi - N^\phi dt)^2 + \frac{1}{B^2} (dr^2 + r^2 d\theta^2) \right], \quad (1)$$

where N , N^ϕ , A and B are four functions of (r, θ) , sometimes represented by their logarithms:

$$\nu := \ln N \quad ; \quad \alpha := \ln A \quad ; \quad \beta := \ln B. \quad (2)$$

Carter (1973, theorem 7) has shown that the most general form of the electric 4-current \mathbf{j} compatible with the hypothesis of stationarity, axisymmetry and circularity has the following components with respect to the (t, r, θ, ϕ) coordinates: $j^\alpha = (j^t, 0, 0, j^\phi)$. He has also shown that the corresponding electromagnetic field tensor \mathbf{F} must be derived from a potential 1-form \mathbf{A} with the following components $A_\alpha = (A_t, 0, 0, A_\phi)$:

$$F_{\alpha\beta} = A_{\beta,\alpha} - A_{\alpha,\beta}. \quad (3)$$

We will not use the “orthonormal” electromagnetic potentials Φ and Ψ introduced in BGS_M but work directly with the components A_t and A_ϕ . A nice feature of A_ϕ is that the magnetic field lines lie on the surfaces $A_\phi = \text{const}$.

For our problem, a privileged observer is the observer \mathcal{O}_0 whose 4-velocity \mathbf{n} is the unit vector normal to the $t = \text{const}$ hypersurfaces (hereafter referred to as the Σ_t hypersurfaces): it corresponds to the observer “at rest with respect to the star's centre” of the Newtonian physics. It is called the *locally nonrotating observer* by Bardeen (1970), the *zero-angular-momentum observer* (ZAMO) by Bardeen (1973), the *Eulerian observer* by Smarr & York (1978) and the *FIDO* by Thorne et al. (1986). The electric field \mathbf{E} and the magnetic field \mathbf{B} as measured by the

observer \mathcal{O}_0 are given by³

$$\begin{aligned} E_\alpha &= F_{\alpha\beta} n^\beta \\ &= \left(0, \frac{1}{N} \left[\frac{\partial A_t}{\partial r} + N^\phi \frac{\partial A_\phi}{\partial r} \right], \frac{1}{N} \left[\frac{\partial A_t}{\partial \theta} + N^\phi \frac{\partial A_\phi}{\partial \theta} \right], 0 \right), \\ B_\alpha &= -\frac{1}{2} \epsilon_{\alpha\beta\mu\nu} n^\beta F^{\mu\nu} \\ &= \left(0, \frac{1}{A^2 B r^2 \sin \theta} \frac{\partial A_\phi}{\partial \theta}, -\frac{1}{A^2 B \sin \theta} \frac{\partial A_\phi}{\partial r}, 0 \right), \end{aligned} \quad (5)$$

where $\epsilon_{\alpha\beta\mu\nu}$ is the Levi-Civita tensor associated with the metric \mathbf{g} . Note that a consequence of Eq. (5) is that the magnetic field lines lie on surfaces $A_\phi = \text{const.}$ In non-relativistic studies, A_ϕ is usually called the *magnetic stream function* or *magnetic flux function* and is denoted a or A (see e.g. Sakurai 1985, Sauty & Tsinganos 1994).

2.2. Maxwell equations

The source-free Maxwell equations $F_{[\alpha\beta;\gamma]} = 0$ are automatically satisfied by the form (3) of \mathbf{F} . The remaining Maxwell equations $F^{\alpha\beta}_{;\beta} = \mu_0 j^\alpha$ can be expressed in terms of A_t and A_ϕ as the Maxwell-Gauss equation

$$\begin{aligned} \Delta_3 A_t &= -\mu_0 \frac{A^4}{B^2} (g_{tt} j^t + g_{t\phi} j^\phi) - \frac{A^4 B^2}{N^2} N^\phi r^2 \sin^2 \theta \times \\ &\quad \times \partial A_t \partial N^\phi - \left(1 + \frac{A^4 B^2}{N^2} r^2 \sin^2 \theta (N^\phi)^2 \right) \times \\ &\quad \times \partial A_\phi \partial N^\phi - (\partial A_t + 2N^\phi \partial A_\phi) \partial (2\alpha + \beta - \nu) \\ &\quad - 2 \frac{N^\phi}{r} \left(\frac{\partial A_\phi}{\partial r} + \frac{1}{r \tan \theta} \frac{\partial A_\phi}{\partial \theta} \right) \end{aligned} \quad (6)$$

and the Maxwell-Ampère equation

$$\begin{aligned} \tilde{\Delta}_3 \tilde{A}^\phi &= -\mu_0 A^8 (j^\phi - N^\phi j^t) r \sin \theta \\ &\quad + \frac{A^4 B^2}{N^2} r \sin \theta \partial N^\phi (\partial A_t + N^\phi \partial A_\phi) \\ &\quad + \frac{1}{r \sin \theta} \partial A_\phi \partial (2\alpha + \beta - \nu), \end{aligned} \quad (7)$$

where

$$\tilde{A}^\phi := \frac{A_\phi}{r \sin \theta}, \quad (8)$$

use has been made of the abridged notation

$$\partial_\alpha \partial_\beta := \frac{\partial \alpha}{\partial r} \frac{\partial \beta}{\partial r} + \frac{1}{r^2} \frac{\partial \alpha}{\partial \theta} \frac{\partial \beta}{\partial \theta}, \quad (9)$$

and Δ_3 and $\tilde{\Delta}_3$ are, respectively, the scalar Laplacian and the ϕ component of the vector Laplacian, in three dimensional flat space:

$$\Delta_3 := \frac{\partial^2}{\partial r^2} + \frac{2}{r} \frac{\partial}{\partial r} + \frac{1}{r^2} \frac{\partial^2}{\partial \theta^2} + \frac{1}{r^2 \tan \theta} \frac{\partial}{\partial \theta} \quad (10)$$

$$\tilde{\Delta}_3 := \frac{\partial^2}{\partial r^2} + \frac{2}{r} \frac{\partial}{\partial r} + \frac{1}{r^2} \frac{\partial^2}{\partial \theta^2} + \frac{1}{r^2 \tan \theta} \frac{\partial}{\partial \theta} - \frac{1}{r^2 \sin^2 \theta} \quad (11)$$

³ Unless otherwise specified, we will refer in the following to E and B as the electric field and the magnetic field, without mentioning “as measured by the observer \mathcal{O}_0 ”.

2.3. Lorentz force and condition for a stationary motion

A first integral of the equation of fluid stationary motion (momentum conservation equation), taking into account the Lorentz force exerted by the electromagnetic field on the conducting medium has been derived in BGSM (Eq. (5.30)); it reads

$$H(r, \theta) + \nu(r, \theta) - \ln \Gamma(r, \theta) + M(r, \theta) = \text{const.}, \quad (12)$$

where

– H is the fluid log-enthalpy defined as

$$H := \ln \left(\frac{e + p}{n m_B c^2} \right), \quad (13)$$

e being the fluid proper energy density, p the pressure, n the proper baryon density, m_B a mean baryon rest mass ($m_B = 1.66 \cdot 10^{-27}$ kg);

– ν is the gravitational potential defined by Eq. (2);

– Γ is the Lorentz factor relating the observer \mathcal{O}_0 and the fluid comoving observer (cf. Eq. (5.6) of BGSM);

– M is the electromagnetic term induced by the Lorentz force.

M is actually a function of A_ϕ only, expressible as

$$M(r, \theta) = M(A_\phi(r, \theta)) = - \int_0^{A_\phi(r, \theta)} f(x) dx, \quad (14)$$

where f is an arbitrary regular function relating the components of the electric current to the electromagnetic potential A_ϕ as an integrability condition of the equation of fluid stationary motion (cf. Eq. (5.29) of BGSM):

$$j^\phi - \Omega j^t = (e + p) f(A_\phi), \quad (15)$$

where Ω is the fluid angular velocity defined as $\Omega := u^\phi / u^t$. We will call f the *current function*. Different choices for f will lead to different magnetic field distributions. Note that in the limit of an incompressible Newtonian body, the integrability condition (15) reduces to the relation derived by Ferraro (1954) [cf. his Eqs. (11) and (14), his function U being exactly our A_ϕ and his function f being $-\mu_0 \rho c^2$ times our function f].

2.4. Perfect conductor relation

According to Ohm’s Law, and assuming that the matter has an infinite conductivity, the electric field as measured by the fluid comoving observer, $E'_\alpha = F_{\alpha\beta} u^\beta$, must be zero. This condition leads to the following relation between the two components of the potential 4-vector inside the star:

$$\frac{\partial A_t}{\partial x^i} = -\Omega \frac{\partial A_\phi}{\partial x^i}. \quad (16)$$

As shown in BGSM, a stationary configuration with a magnetic field is necessarily *rigidly* rotating (i.e. has $\Omega =$

const.). Consequently, Eq. (16) is integrated immediately to

$$A_t = -\Omega A_\phi + C, \quad (17)$$

where C is a constant. The choice of C will fix the total electric charge of the star. Note that Eq. (17) holds inside the star only.

2.5. Global quantities

The magnetic dipole moment \mathcal{M} is given by the leading term of the asymptotic behaviour of the magnetic field as measured by \mathcal{O}_0 :

$$B_{(r)} \sim_{r \rightarrow \infty} \frac{\mu_0}{2\pi} \frac{\mathcal{M} \cos \theta}{r^3}; \quad B_{(\theta)} \sim_{r \rightarrow \infty} \frac{\mu_0}{4\pi} \frac{\mathcal{M} \sin \theta}{r^3}, \quad (18)$$

$B_{(r)}$ and $B_{(\theta)}$ being the component of \mathbf{B} in the orthonormal basis associated to (r, θ, ϕ) . They are related to the components B_r and B_θ given in Eq. (5) by

$$B_{(r)} = \frac{B}{A^2} B_r; \quad B_{(\theta)} = \frac{B}{A^2 r} B_\theta. \quad (19)$$

The total electric charge of the star, Q , is given by the leading term of the asymptotic behaviour of the electric field as measured by \mathcal{O}_0 :

$$E_{(r)} \sim_{r \rightarrow \infty} \frac{\mu_0}{4\pi} \frac{Q}{r^2}; \quad E_{(\theta)} \sim_{r \rightarrow \infty} \frac{\mu_0}{4\pi} \frac{Q}{r^2}. \quad (20)$$

Equivalently, Q is expressible as

$$Q = \int_{\Sigma_t} j^\mu \epsilon_{\mu\alpha\beta\gamma} + Q_{\text{surf}} \quad (21)$$

$$= \int \frac{NA^6}{B} j^t r^2 \sin \theta dr d\theta d\phi + Q_{\text{surf}}, \quad (22)$$

where Q_{surf} is the surface charge.

3. The numerical procedure and its tests

We describe here only the electromagnetic part of the code. For the fluid and gravitational part, we refer to BGSM. Let us simply recall that our code is based on an iterative procedure, each step consisting in solving Poisson equations by means of a Chebyshev-Legendre spectral method developed by Bonazzola & Marck (1990). Typically the computations have been performed with 41 Chebyshev coefficients in r and 21 coefficients in θ .

3.1. Numerical resolution of the electromagnetic equations

In order to obtain a solution of the equations presented in Sect. 2, one needs to specify a value for the central log-enthalpy H , a value for the angular velocity Ω , and a value for the total electric charge Q (possibly $Q = 0$). (An alternative scheme could be, instead of fixing Q , to impose $\mathbf{E} \cdot \mathbf{B} = 0$ as a boundary condition at the surface of the star

in order to mimic a magnetosphere; the solution would be then an approximate one outside the star, which is not the case in the procedure described below). One needs also to pick a choice for the current function f .

The iterative procedure is then as follows. At the first step, A_ϕ is set identically to zero. At a given step, a value 0A_t of A_t inside the star is deduced from the value of A_ϕ at the previous step by the perfect conductivity equation (17), setting the constant C to zero. Then one computes the Laplacian of 0A_t and use the Maxwell-Gauss equation (6) to obtain the value of the charge density j^t inside the star (using for the j^ϕ which appears in Eq. (6) its value at the previous step). The current density component j^ϕ is then deduced from j^t and the previous value of A_ϕ via the function f and Eq. (15). Then one solves the Maxwell equations (6) and (7) by considering them as two *linear* Poisson equations for A_t and \tilde{A}_ϕ , with a fixed right-hand side: this latter is calculated from the newly determined j^t and j^ϕ and the previous step values of A_t and A_ϕ (in the non-linear terms containing ∂A_t and ∂A_ϕ). For \tilde{A}_ϕ , the boundary condition⁴ $A_\phi = 0$ at $r = +\infty$ is used. We then obtain a unique smooth solution for A_ϕ . For A_t the procedure is a little more complicated since in general a rotating perfect conductor is endowed with a surface charge density, so that the component of the electric field normal to the surface is discontinuous, meaning that the electric potential A_t is not differentiable across the surface. We then solve the equation for A_t in two steps: (i) a solution 1A_t to the Poisson equation (6) is obtained outside the star with the boundary condition ${}^1A_t = 0$ at $r = +\infty$. This solution, is by no means unique, since any harmonic function ψ (i.e. satisfying $\Delta_3 \psi = 0$) vanishing at infinity can be added to 1A_t . (ii) an harmonic function of the form

$$\psi(r, \theta) = \sum_{l=0}^L a_l \frac{P_l(\cos \theta)}{r^{l+1}}, \quad (23)$$

where P_l is the Legendre polynomial of degree l , is added to 1A_t outside the star so that ${}^0A_t := {}^1A_t + \psi$ matches, on the star's surface, the value of 0A_t inside the star which has been determined previously by the perfect conductor relation ${}^0A_t = -\Omega A_\phi$. Technically the matching is achieved by solving a linear system for the $L + 1$ coefficients a_l of the expansion (23), $L + 1$ being the number of grid points on the star's surface (number of collocation points in θ). The solution 0A_t obtained in this way is continuous in all space but not necessarily differentiable across the star's surface. Besides, this solution has a certain electric charge, 0Q say, given by Eq. (20) and which does not a priori coincide with the desired electric charge Q . The arbitrary nature of the constant C of Eq. (17) can be used to adjust the electric charge, 0A_t having been obtained by setting

⁴ as explained in BGSM, our numerical grid extends to $r = +\infty$ thank to a change of coordinate $u = 1/r$ in the space outside the star.

$C = 0$. This is achieved by considering the following solution of the equation $\Delta_3 {}^2A_t = 0$: ${}^2A_t = 1$ inside the star and 2A_t has the same form as the function ψ of Eq. (23) outside the star, the coefficients a_l being determined in order to insure the continuity of 2A_t across the star's surface. Let 2Q be the electric charge associated with 2A_t . The constant C is then determined by

$$C = \frac{Q - {}^0Q}{{}^2Q} \quad (24)$$

and the final solution for A_t is

$$A_t = {}^0A_t + C = -\Omega A_\phi + C \quad \text{inside the star} \quad (25)$$

$$A_t = {}^0A_t + C {}^2A_t \quad \text{outside the star} . \quad (26)$$

By construction A_t satisfies the Poisson equation (6) (with the right-hand computed from values at the previous step) and corresponds to the required electric charge Q .

Once A_t and A_ϕ are obtained, the electric and magnetic fields are computed via Eqs. (4) and (5). The electromagnetic stress-energy tensor is then deduced from Eq. (5.32) of BGSM and put as a source term, beside the fluid stress-energy tensor, in the Einstein equations giving the gravitational field (Eqs. (3.19)-(3.22) of BGSM).

3.2. Tests of the numerical code

Various tests have been performed on the electromagnetic part of the code (for the gravitational part we refer to BGSM), mainly by comparing numerical solutions to exact ones for simple charge and current distributions.

3.2.1. Rotating magnetic dipole

We have considered an electrostatic dipole, a magnetostatic dipole and a rotating magnetic dipole, all of them in flat space (no gravitation). Let us detail the results for the rotating magnetic dipole, since they are representative of the precision achieved in all other cases.

By ‘‘rotating magnetic dipole’’, we mean two different physical situations: (i) a conducting sphere in rotation with surface electric currents and (ii) a conducting sphere in rotation with an infinitely small electric current loop at the origin. In case (i), the current distribution is modelled by

$$j^{(\phi)}(r, \theta) = j_0 r \sin \theta \exp\left(-\frac{(r-R)^2}{\delta^2}\right), \quad (27)$$

where j_0 is a constant, R is the sphere's radius and δ is the width of the distribution, which we do not put to zero in order to have only smooth functions. Typically, we use $\delta \sim .01 R$. The exact solution for (\mathbf{E}, \mathbf{B}) (corresponding to $\delta = 0$) may be found in Ruffini & Treves (1973). The magnetic field is uniform and parallel to the rotation axis inside the sphere and dipolar outside. The electric field

outside the sphere is the sum of a monopolar term and a quadrupolar one.

In case (ii), the current distribution is modelled by

$$j^{(\phi)}(r, \theta) = j_0 r \sin \theta \exp\left(-\frac{r^2}{\delta^2}\right). \quad (28)$$

The exact solution (corresponding to $\delta = 0$, i.e. to a point magnetic dipole moment) may be found in the Table 4.1 of Michel (1991)⁵. The magnetic field is dipolar in all space. The electric field outside the sphere is the sum of a monopolar term and a quadrupolar one. The difference between the exact solution and the solution given by the numerical code is depicted in Fig. 1 in the case of a conducting sphere of diameter 1 m, rotating at the angular velocity $\Omega = 3000 \text{ rad s}^{-1}$, with a central loop current $j_0 = 10^{11} \text{ A m}^{-2}$. Near the star's centre, the discrepancy is quite important because the current distribution used in the code is not exactly a point dipole ($\delta \neq 0$). But at half the stellar radius, the relative error becomes less than 10^{-5} and is of the order $\sim 10^{-9}$ outside the star.

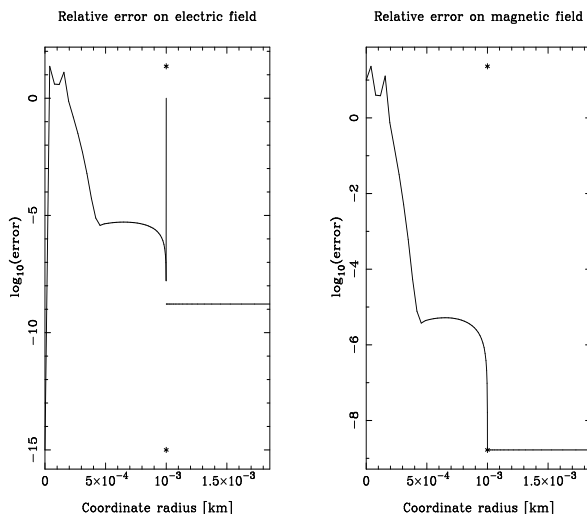


Fig. 1. Comparison between the exact solution and the numerical one in the case of a rotating conducting sphere with a point magnetic dipole moment at its centre. The left figure corresponds to the electric field, the error being defined as the square root of $[(E_{(r)} - E_{(r)}^{\text{exact}})^2 + (E_{(\theta)} - E_{(\theta)}^{\text{exact}})^2] / [(E_{(r)})^2 + (E_{(\theta)})^2]$. The right figure depicts the same thing for the magnetic field. Asterisks denote the sphere's surface.

3.2.2. Comparison with Ferraro's solution

Ferraro (1954) has obtained an analytical solution for a Newtonian incompressible fluid body with an electric current distribution corresponding to the choice $f(x) = \text{const}$

⁵ in this reference, the term $2/3r$ in the seventh line should read $2/3r^2$

for the current function of Eq. (15). Ferraro’s solution is valid for a body whose shape remains close to a sphere and reads

$$A_\phi = -\mu_0 \rho c^2 f_0 (r^2/10 - R^2/6) r^2 \sin^2 \theta \quad \text{for } r \leq R \quad (29)$$

$$A_\phi = \mu_0 \rho c^2 f_0 \frac{R^5}{15r} \sin^2 \theta \quad \text{for } r \geq R, \quad (30)$$

where f_0 is the constant value taken by the current function f and R is the stellar radius. The discrepancy between Ferraro’s solution and the numerical one resulting from the code is depicted in Fig. 2. It is everywhere less than 10^{-3} , being less than 5×10^{-4} inside the star. These numbers are higher than those of the test of Sect. 3.2.1 but one should keep in mind that Ferraro’s solution is only an approximate one, assuming no deviation from spherical symmetry, whereas the numerical solution takes into account the deformation of the star by Lorentz forces. Of course, in order to perform the test, we have considered a magnetic field weak enough for Ferraro’s approximation to be valid, as well as a very weak gravitational field for the Newtonian approximation to be justified: the tested configuration is a $2.67 \times 10^{-2} M_\odot$ star of (constant) density $1.66 \times 10^9 \text{ kg m}^{-3}$ with a polar magnetic field $B_{\text{pole}} = 6.6 \times 10^5 \text{ T}$.

Ferraro’s solution is interesting since it allows to test the response of the star to the magnetic field, contrary to the tests of Sect. 3.2.1. The deformation of the star as computed by Ferraro at first order around the spherical symmetry, is given in terms of the polar magnetic field by the eccentricity

$$\epsilon = \frac{15}{4} \frac{B_{\text{pole}}}{\sqrt{\pi G \mu_0} \rho R}. \quad (31)$$

For the configuration considered above, $\epsilon = 0.04670$. The eccentricity resulting from the code is 0.04683, so that the relative discrepancy is 3×10^{-3} . Here again let us recall that Ferraro’s solution is only an approximate one, so that this value reflects not only the true numerical error but also Ferraro’s error with respect to the exact solution. Nevertheless the very good agreement with Ferraro’s solution means that the action of Lorentz forces upon the fluid is correctly treated by the code and in particular that there is no error in the conversion from magnetic units to fluid units.

3.2.3. Virial identities

A different kind of test is provided by the virial identities GRV2 (Bonazzola & Gourgoulhon 1994) and GRV3 (Gourgoulhon & Bonazzola 1994), the latter being a relativistic generalization of the Newtonian virial theorem. GRV2 leads to the $|1 - \lambda|$ error indicator introduced in BGSM. These virial identities allow to test each computation and not only the simplified ones presented above. It notably controls the convergence of the iterative procedure used in the code. In most of our calculations, the final

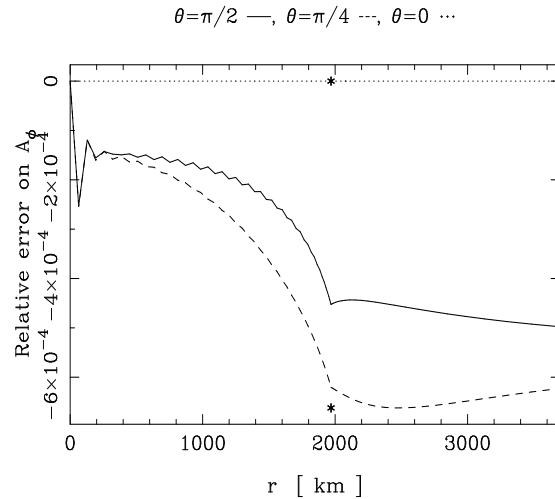


Fig. 2. Comparison between Ferraro’s analytical solution and the numerical one in the case of a Newtonian incompressible fluid endowed with a magnetic field corresponding to the current function $f(x) = \text{const}$. The plotted quantity is the relative difference between the two values of A_ϕ as a function of the radial coordinate r for three values of θ . Asterisks denote the star’s surface.

value of the GRV2 or GRV3 error indicator is of the order 10^{-5} (polytropic EOS) or a few 10^{-4} (tabulated EOS). Let us recall that tabulated EOS introduce an important numerical error because they do not strictly obey to the thermodynamical relations (cf. Sect. 4.2 of Salgado et al. 1994). We systematically rejected any solution for which the GRV2 or GRV3 error is greater than 10^{-2} , such a relative error being too large for considering that the numerical procedure has converged. This may happen if the magnetic field is too large for any stationary configuration to exist.

4. Static magnetized configurations

In order to investigate some purely magnetic effects on stellar configurations, let us first consider the case of static (i.e. non rotating) neutron stars. More precisely, a *static* spacetime (in the sense of the time Killing vector being hypersurface-orthogonal) implies not only a non rotating fluid ($\Omega = 0$) but also a vanishing electric charge. Only in this case the electric field as measured by \mathcal{O}_0 is zero. On the contrary, a non-vanishing electric charge creates an electrostatic field outside the star, so that there exists a net electromagnetic momentum density vector $\mathbf{E} \times \mathbf{B} / 2\mu_0$ which generates a non-zero angular momentum, though the fluid does not rotate [Feynman’s disk paradox (Feynman et al. 1964, Ma 1986, de Castro 1991)]. Consequently the shift vector component $N^\phi \neq 0$ and the spacetime is not static. We observed this effect numerically but only for huge values of the electric charge: $Q \sim 10^{17} \text{ C}$.

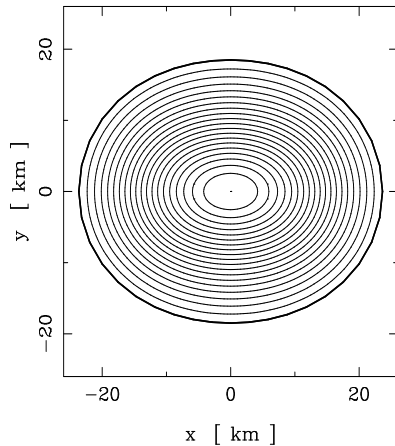


Fig. 3. Fluid proper density isocontours in the (r, θ) plane of a static magnetized star of $2.98 M_{\odot}$ built on the Pol2 EOS of Salgado et al. (1994a) (polytropic EOS with $\gamma = 2$) with a current function $f(x) = \text{const.} = 4 \times 10^{15}/R \text{ A m}^{-2} \rho_{\text{nuc}}^{-1} \text{c}^{-2}$, where R is the r coordinate of the star's equator. The central energy density is $e = 1.42 \rho_{\text{nuc}} \text{c}^2$ ($1 \rho_{\text{nuc}} := 1.66 \times 10^{17} \text{ kg m}^{-3}$).

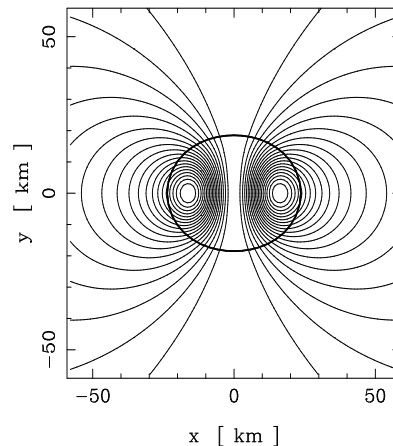


Fig. 4. Magnetic field lines in the (r, θ) plane for the static star configuration corresponding to Fig. 3. The thick line denotes the star's surface. The magnetic field amplitude is $B_c = 3.57 \times 10^4 \text{ GT}$ at the star's centre and $B_{\text{pole}} = 9.1 \times 10^3 \text{ GT}$ at the north pole; the magnetic dipole moment is $\mathcal{M} = 5.42 \times 10^{32} \text{ A m}^2$.

4.1. Deformation of the star

Even in the static case, the stress-energy tensor of the electromagnetic field is not isotropic (cf. Eq. (5.33) of BGSF with $U = 0$) so that the star deviates from spherical symmetry. For large magnetic field this deviation becomes important as shown in Fig. 3. The corresponding magnetic field lines are plotted in Fig. 4. Note that the situation depicted in Figs. 3 and 4 corresponds to an important magnetic field: $B_{\text{pole}} = 9.1 \times 10^3 \text{ GT}$. The flattened shape is a general result for a magnetized configuration. We thus may conclude that the Lorentz forces exerted by the electromagnetic field on the conducting fluid behave as centrifugal forces. Note that the flattening property of the magnetic field has been recognized long ago (in the Newtonian case) by Chandrasekhar & Fermi (1953).

4.2. Maximum values of the magnetic field

If the value of the central magnetic field is high enough for the magnetic pressure equals the fluid pressure p , then the total stress tensor S_{ij} has a vanishing component along the symmetry axis, as it can be seen by combining Eq. (5.7c) and (5.32c) of BGSF:

$$S_r{}^r = p + \frac{1}{2\mu_0} (B_{\theta}B^{\theta} - B_rB^r) , \quad (32)$$

with, on the symmetry axis near the centre, $B_{\theta}B^{\theta} = 0$ and $B_rB^r/2\mu_0 \simeq p$. Hence $S_r{}^r = 0$. Away from the centre, the fluid pressure decreases more rapidly than the magnetic pressure along the symmetry axis, so that $S_r{}^r < 0$,

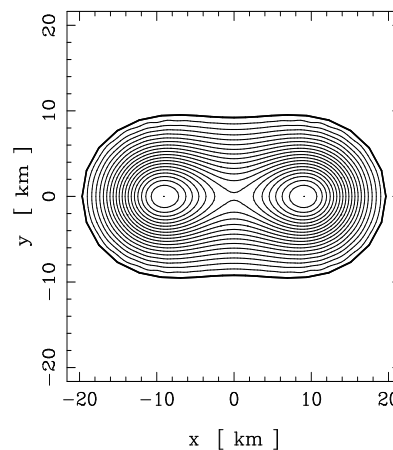


Fig. 5. Fluid proper density isocontours in the (r, θ) plane for the maximum mass static magnetized star built on the Pol2 EOS of Salgado et al. (1994a) (polytropic EOS with $\gamma = 2$). The current function $f(x) = \text{const.} = 5.63 \times 10^{15}/R \text{ A m}^{-2} \rho_{\text{nuc}}^{-1} \text{c}^{-2}$, where R is the r coordinate of the star's equator. The central energy density is $e = 1.42 \rho_{\text{nuc}} \text{c}^2$ and the mass $M = 4.06 M_{\odot}$; the other characteristics are listed on the third line of Table 1.

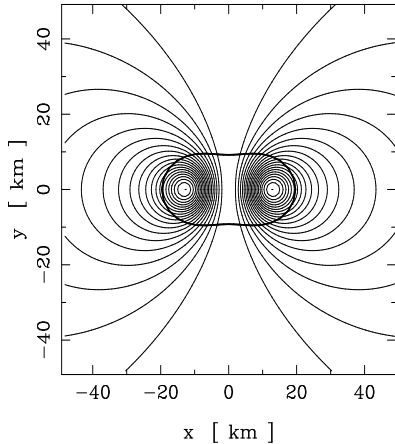


Fig. 6. Magnetic field lines in the (r, θ) plane for the maximum mass configuration corresponding to Fig. 5. The thick line denotes the star's surface. The magnetic field amplitude is $B_c = 9.00 \times 10^4$ GT at the star's centre and $B_{\text{pole}} = 4.57 \times 10^4$ GT at the north pole; the magnetic dipole moment is $\mathcal{M} = 1.12 \times 10^{33}$ Am².

which means that the fluid + magnetic field medium develops some *tension* instead of *pressure* along the symmetry axis. The star displays then a pinch along the symmetry axis, as it can be seen on Figs. 5 and 6. The fact that in this case the magnetic pressure exceeds the fluid pressure everywhere on the symmetry axis can be clearly seen in Fig. 7 (dotted line), which represents the ratio of the two pressures throughout the star. For magnetic fields higher than that presented in Figs. 5-7, no stationary configuration can exist and the numerical procedure described in Sect. 3.1 fails to converge.

The stellar shape displayed in Fig. 5 is a typical feature of the maximum allowable magnetic field and is not due to the fact that this particular configuration is the maximum mass one or that the EOS is Pol2. Indeed, we found very similar shapes for all central densities in the explored range ($0.15\rho_{\text{nuc}}$ up to $5\rho_{\text{nuc}}$) and all EOS when the magnetic field has reached the maximum value for which a solution could be obtained. In all cases, the ratio of $B^2/2\mu_0$ to p was close to 1 at the star's centre (cf. the sixth column of Table 1).

Note that the maximum values of B_{pole} are four orders of magnitude higher than the maximum observed value: $B_{\text{pole}} = 2.1$ GT in the pulsar PSR B0154+61 (Taylor et al. 1993), which means that the magnetic field in the observed pulsar is not limited by the condition of stellar equilibrium but by the physical processes it originates from.

$\theta=\pi/2$ —, $\theta=\pi/4$ ---, $\theta=0$...

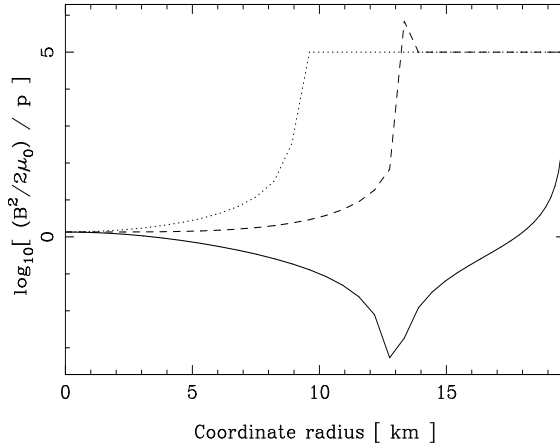


Fig. 7. Ratio of the magnetic pressure $B^2/2\mu_0$ to the fluid pressure p as a function of the radial coordinate r and along three angular directions for the maximum mass configuration displayed in Figs. 5 and 6. Outside the star, where $p = 0$, the logarithm of the ratio has been set to 5. At the star's centre, $(B^2/2\mu_0)/p = 1.36$.

4.3. Effect of the magnetic field on M_{max}

In order to investigate the effect of the magnetic field on the maximum mass of static configurations, we choose the simplest form of the current function:

$$f(x) = \text{const.} = f_0, \quad (33)$$

and vary f_0 from 0 (no magnetic field) up to the maximal value for which the code converges and for which the ratio of the magnetic pressure to the fluid pressure at the star's centre come close to one (cf. sixth column of Table 1). The choice (33) results in electric currents concentrated deep inside the star, with the same behaviour as that represented in Fig. 10 for the rotating case. Each static configuration is determined by the value of the central log-enthalpy H_c and the value of f_0 . In the plane (H_c, f_0) , we followed curves of constant magnetic dipole moment \mathcal{M} and determined for each of them the maximal gravitational mass.

This study has been conducted for five of the EOS used in Salgado et al. (1994a,b): Pol2 ($\gamma = 2$ polytrope), DiazII (model II of Diaz Alonso 1985), PandN (pure neutron model of Pandharipande 1971), BJI (model IH of Bethe & Johnson 1974) and HKP (Haensel et al. 1981). For details about these EOS, the reader may consult Sect. 4.1 of Salgado et al. (1994a).

Some results are presented in Table 1 which gives maximum mass configurations (i) with no magnetic field (first line), (ii) with some fixed magnetic dipole moment (second line), (iii) among all magnetized configurations (third line).

Different behaviours appear for different EOS: the maximum gravitational mass at fixed magnetic dipole moment \mathcal{M} as well as the maximum baryon number at fixed \mathcal{M} are both increasing functions of \mathcal{M} for the EOS DiazII (cf. Fig. 8), whereas the maximum baryon number is a decreasing function of \mathcal{M} for the EOS BJI (cf. Fig. 9), the maximum mass remaining a increasing function. Pol2 models behave as DiazII ones, whereas PandN and HKP models behave as BJI ones. In all cases, the maximum gravitational mass increases with the magnetic field, by 28.6% for Pol2, 20.2% for DiazII, 14.9% for PandN, 17.3% for BJI, and 13.3% for HKP (compare first and third lines in Table 1).

5. Rotating magnetized configurations

5.1. Electric charge

As we have seen in Sect. 2 and 3.1, the total electric charge Q is a freely specifiable parameter of our models. Realistic neutron stars certainly possess a net electric charge, which may be of the order of 10^{12} C (Michel 1991, Chap. 4 and Cohen et al. 1975). The key point is that this (huge) charge is compensated by the charge provided by the magnetospheric particles to lead to globally neutral star + magnetosphere system. Now, as stated in Sect. 1, we do not attempt to model any filled magnetosphere and consider neutron stars surrounded by matter vacuum. In consequence, we do not try to give a specific charge to our models (this would require a detailed magnetosphere model) and consider globally neutral stellar configurations: $Q = 0$. Anyway, the effect of a non-zero value of Q on the non-electromagnetic characteristics of the star reveals to be extremely small: we verified that

$$\forall H_c, \Omega, \quad |M(H_c, \Omega, Q = 10^{18} \text{ C}) - M(H_c, \Omega, Q = 0)| \leq 10^{-5} M_\odot, \quad (34)$$

which is of the order of the numerical error committed by the code. The global quantity which is the most sensitive to a non-zero value of Q is the angular momentum as mentioned in Sect. 4. In the rotating case however the fluid angular momentum dominates by at least one order of magnitude the electromagnetic angular momentum, even for huge values of Q ($Q \sim 10^{18}$ C).

5.2. Structure of the electromagnetic field

In order to consider different electric current distributions, concentrated around the star's centre or not, we use different choices for the current function f . The most immediate choice is (33) ($f(x) = f_0 = \text{const}$). The resulting electric current distribution is shown in Fig. 10 for a Pol2 $M = 3.37 M_\odot$ model rotating at $\Omega = 3 \times 10^3 \text{ rad s}^{-1}$. $j^{(\phi)}$ has a maximum at one third of the stellar radius. The resulting magnetic field is shown in Fig. 11 and 13. The magnetic field amplitude has a maximum near the star's

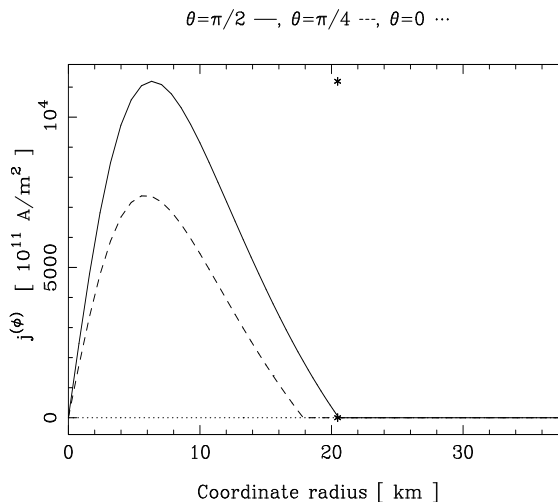


Fig. 10. Electric current distribution induced by the current function $f(x) = \text{const.} = 10^{15}/R \text{ A m}^{-2} \rho_{\text{nuc}}^{-1} c^{-2}$ for a Pol2 EOS model, of central energy density $e_c = 3.06 \rho_{\text{nuc}} c^2$, rotating at $\Omega = 3 \times 10^3 \text{ rad s}^{-1}$. The plotted quantity is the value $j^{(\phi)}$ of the azimuthal component of j in an orthonormal basis in the equatorial plane $\theta = \pi/2$ (solid line), along $\theta = \pi/4$ (dashed line) and along the rotation axis $\theta = 0$ (dotted line). Asterisks denote the star's equatorial radius.

centre, the surface value being approximately four times lower. The dominant dipolar structure of \mathbf{B} clearly appears in Fig. 13, as if \mathbf{B} was generated by a single current loop located inside the star. The induced electric field is represented in Figs. 12 and 13. Note on Fig. 12 the discontinuity in the component of \mathbf{E} normal to the star's surface, due to surface charges. The cusp across the surface in the component $E_{(\theta)}$ along the radius $\theta = \pi/4$ is due to the discrepancy between $E_{(\theta)}$ and the component of \mathbf{E} tangential to the surface (resulting from the non-spherical shape of the star), this latter being perfectly smooth, as expected. The fact that A_t is continuous but not differentiable across the star's surface, because of the surface charges, is clear on Fig. 13. Note also on Fig. 13 that, inside the star, the lines $A_t = \text{const}$ coincide with the magnetic field lines, as expected from the perfect conductor relation (17) and the fact that the magnetic field lines are the lines $A_\phi = \text{const}$. (cf. Sect. 2.1).

In order to get current distributions different from the one described above, we have considered the following forms of the current function, beside the constant form (33),

$$f(x) = \frac{\alpha}{1+x}, \quad x = \frac{A_\phi}{A_\phi^0} \quad (35)$$

$$f(x) = \alpha \left(1 - \frac{1}{(\beta x)^2 + 1} \right), \quad x = \frac{A_\phi}{A_\phi^0}, \quad (36)$$

Table 1. Maximum mass (at fixed magnetic dipole moment) neutron stars in the non-rotating case. For each EOS, the last line is the maximum mass configuration among all static magnetized models. \mathcal{M} is the magnetic dipole moment, B_c and B_{pole} are respectively the values of the magnetic field at the centre and the north pole of the star, H_c is the central value of the log-enthalpy as defined by Eq. (13), e_c the central energy density ($1 \rho_{\text{nuc}} := 1.66 \cdot 10^{17} \text{ kg m}^{-3}$), $p_{\text{mg},c}/p_{\text{fl},c}$ the ratio of the magnetic pressure to the fluid pressure at the star centre, M the gravitational mass, \mathcal{B} the baryon mass, E_{bind} the binding energy per baryon (with the convention $E_{\text{bind}} < 0$ for a bound configuration), R_{circ} the circumferential radius (length of the star’s equator divided by 2π) and GRV2 and GRV3 the estimates of the global numerical relative error provided by the virial identities GRV2 and GRV3 (cf. text). We use $G = 6.6726 \cdot 10^{-11} \text{ m}^3 \text{ kg}^{-1} \text{ s}^{-2}$ and $1 M_{\odot} = 1.989 \cdot 10^{30} \text{ kg}$.

EOS	$\mathcal{M} [10^{32} \text{ A m}^2]$	$B_c [10^3 \text{ GT}]$	$B_{\text{pole}} [10^3 \text{ GT}]$	H_c	$e_c [\rho_{\text{nuc}} c^2]$	$\frac{p_{\text{mg},c}}{p_{\text{fl},c}}$	$M [M_{\odot}]$	$\mathcal{B} [M_{\odot}]$	$E_{\text{bind}} [m_{\text{B}} c^2]$	$R_{\text{circ}} [\text{km}]$	GRV2	GRV3
Pol2	0	0	0	0.491	4.17	0	3.158	3.470	-0.0897	21.77	1E-14	4E-12
	2.00	37.8	6.2	0.483	4.07	0.04	3.182	3.486	-0.0872	21.93	1E-06	2E-06
	11.22	90.0	45.7	0.225	1.42	1.36	4.062	4.279	-0.0507	26.45	1E-03	7E-04
DiazII	0	0	0	0.610	15.21	0	1.933	2.210	-0.1253	10.92	1E-04	1E-04
	0.50	73.8	14.1	0.600	14.85	0.03	1.940	2.212	-0.1229	11.00	2E-04	2E-04
	3.08	207.4	108.3	0.285	6.22	1.10	2.324	2.508	-0.0734	13.12	1E-04	9E-05
PandN	0	0	0	0.733	24.39	0	1.662	1.932	-0.1340	8.55	1E-04	2E-04
	0.20	64.7	11.9	0.727	24.13	0.01	1.663	1.931	-0.1384	8.57	1E-04	2E-04
	1.86	302.8	153.8	0.350	11.21	1.01	1.910	2.064	-0.0746	10.00	3E-04	2E-04
BJI	0	0	0	0.699	18.64	0	1.856	2.134	-0.1303	9.91	2E-06	3E-06
	0.30	61.5	11.0	0.692	18.40	0.01	1.858	2.132	-0.1288	9.94	2E-06	2E-06
	2.63	233.2	121.0	0.300	7.47	1.10	2.176	2.344	-0.0717	12.05	1E-04	5E-05
HKP	0	0	0	0.725	8.75	0	2.836	3.422	-0.1712	13.67	1E-04	8E-05
	0.80	56.0	12.4	0.714	8.57	0.02	2.840	3.417	-0.1689	13.75	1E-04	9E-05
	4.90	196.6	104.5	0.370	4.36	0.90	3.212	3.594	-0.1063	15.85	6E-04	3E-04

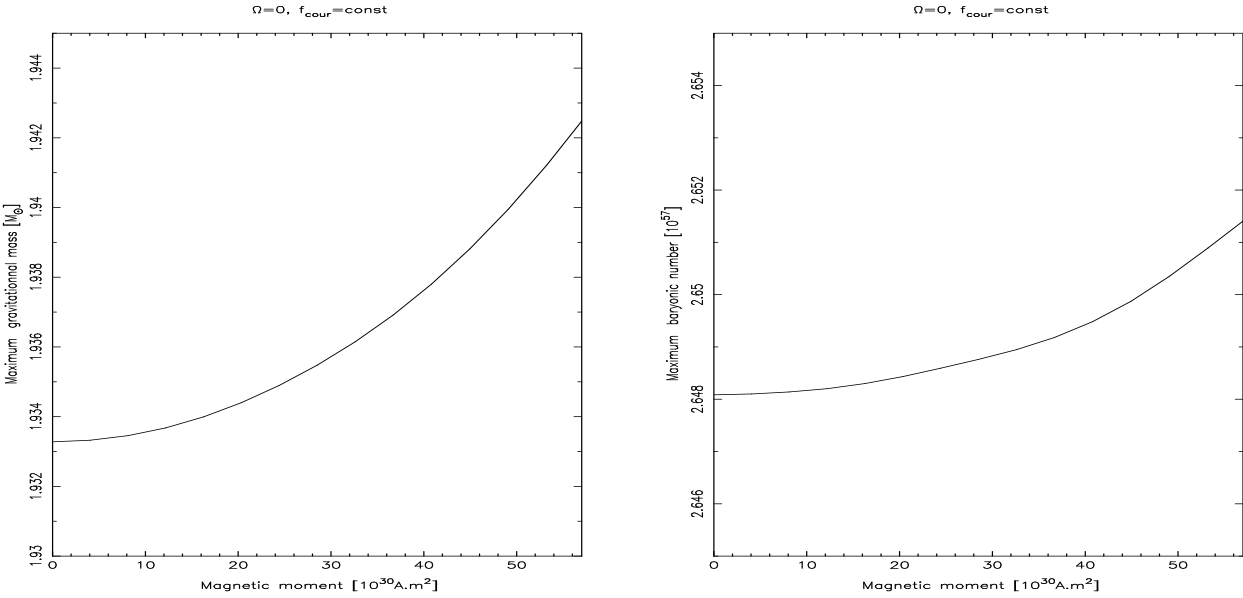


Fig. 8. Maximum gravitational mass (left) and maximum baryon number (right) along static sequences at fixed magnetic dipole moment as a function of the magnetic dipole moment for the DiazII EOS .

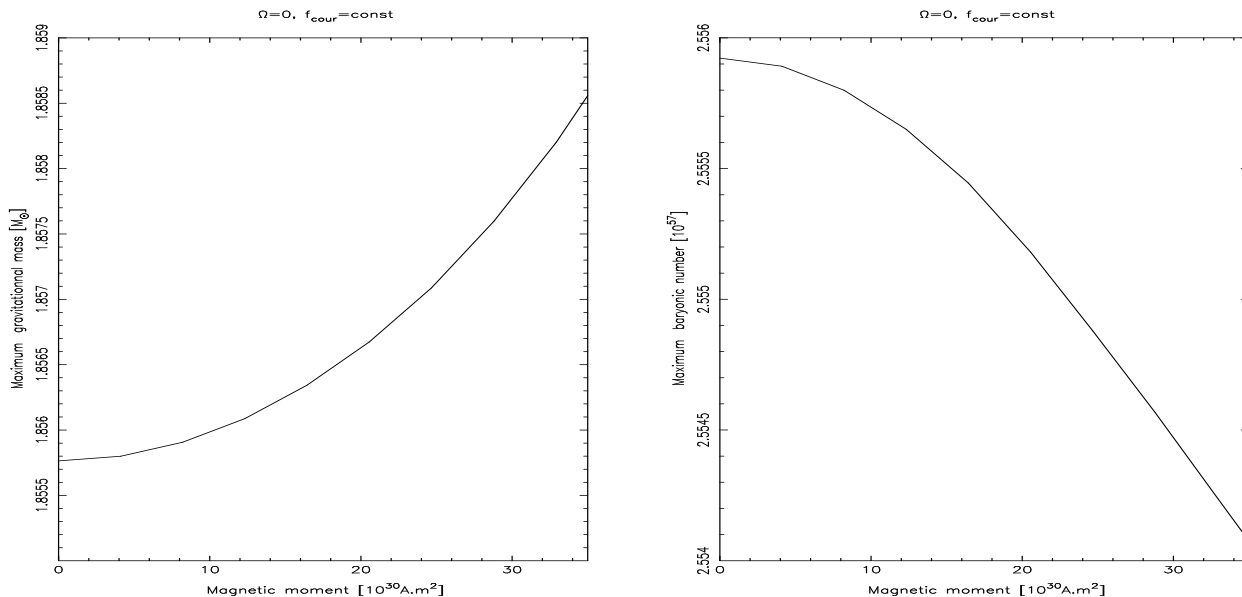


Fig. 9. Same as Fig. 8 but for the BJI EOS .

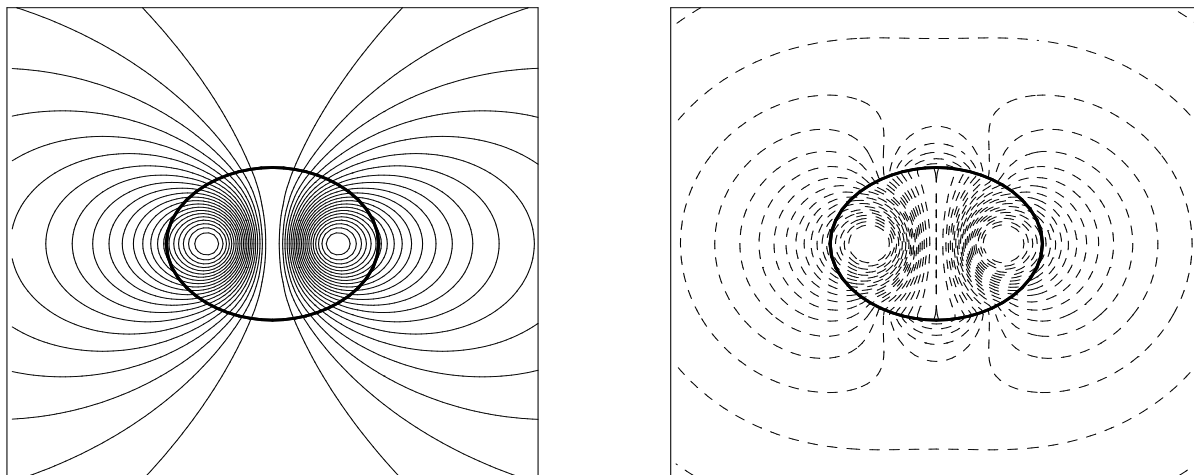


Fig. 13. Magnetic field lines (left) and electric isopotential lines $A_t = \text{const}$ (right) in the (r, θ) plane for the configuration considered in Figs. 10, 11 and 12. The thick line denotes the star's surface.

where $A_\phi^0 = 4\pi \times 10^4 R^3 \text{ T m}^{-1}$, R being the value of the coordinate r at the equator. One might think about other choices, such as $f(x) = \alpha x + \beta$, $f(x) = \alpha x^2$, or $f(x) = \alpha/(1+x^2)$, but with such functions, the iterative procedure described in Sect. 3.1 revealed not to converge, resulting in a solution either cyclic or chaotic with respect to the number of steps. This behaviour is not due to some numerical instability but results from the non-linear coupling between j^ϕ and A_ϕ via the Eqs. (7) and (15), which may be written schematically as a unique equation $\Delta A_\phi = F(A_\phi)$. Now it is well known that some sequences defined by an iterative relation $u_{n+1} = F(u_n)$ may exhibit

a cyclic and/or chaotic behaviour when f is non-linear and not one-to-one [take $F(x) = 4\alpha(x-x^2)$, which generates cycles of increasing order for $0.75 < \alpha < 0.892$ and chaotic sequences for $\alpha > 0.892$]. For this reason, we did not consider the current functions mentioned above in our study.

The choice (35) leads to a current distribution slightly different from that corresponding of $f(x) = \text{const}$. (Fig. 10), being simply more concentrated towards the star's centre, especially in the direction of the equatorial plane. The resulting electromagnetic field is very similar to that of Figs. 11-13.

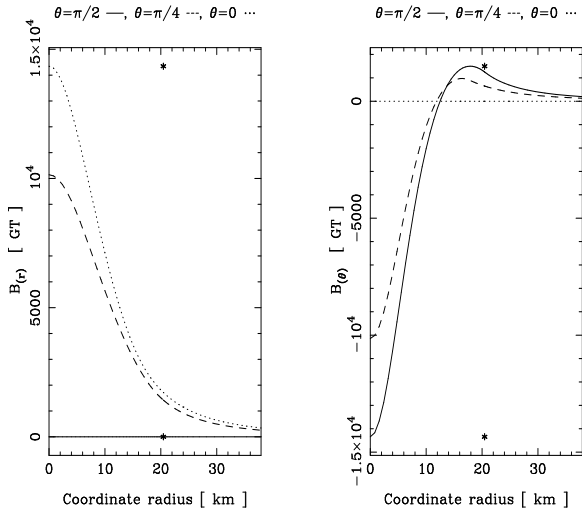


Fig. 11. Components $B_{(r)}$ (left) and $B_{(\theta)}$ (right) of the magnetic field generated by the electric current distribution of Fig. 10. The notations are the same as in Fig. 10.

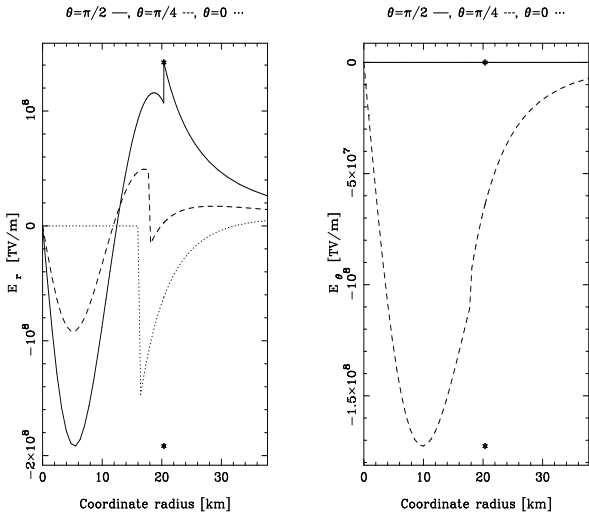


Fig. 12. Components $E_{(r)}$ (left) and $E_{(\theta)}$ (right) of the electric field corresponding to the configuration of Figs. 10 and 11. The notations are the same as in Fig. 10. On the right figure, the dotted line merges with the solid one.

The choice (36) leads to a current distribution which is represented in Fig. 14. There is no current around the centre and the maximum of the distribution is reached at almost half of the stellar radius. The resulting magnetic field is shown in Fig. 15. The difference with that generated by $f(x) = \text{const}$ (cf. Fig. 11) is not important; simply the maximum of \mathbf{B} is achieved apart from the star's centre (except near the rotation axis). The corresponding electric field is shown in Fig. 16. It has more or less the same structure as that of Fig. 12.

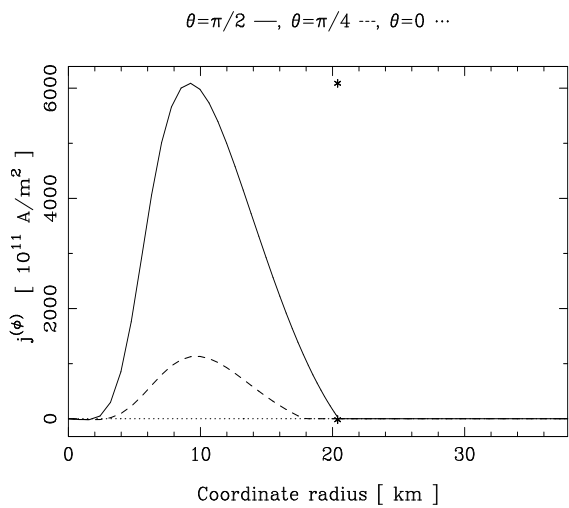


Fig. 14. Electric current distribution induced by the choice $f(x) = 10^4 [1 - 1 / ((3.3 \times 10^{-3} x)^2 + 1)] / R \text{ A m}^{-2} \rho_{\text{nuc}}^{-1} c^{-2}$ for a Pol2 EOS model, of central energy density $e_c = 3.06 \rho_{\text{nuc}} c^2$, rotating at $\Omega = 3 \times 10^3 \text{ rad s}^{-1}$. The notations are the same as in Fig. 10.

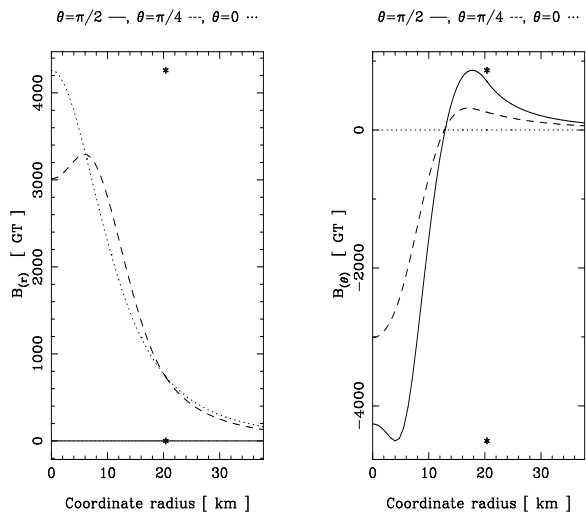


Fig. 15. Components $B_{(r)}$ (left) and $B_{(\theta)}$ (right) of the magnetic field generated by the electric current distribution of Fig. 14. The notations are the same as in Fig. 10.

5.3. Differences between magnetized and non-magnetized configurations

For a given EOS and a given choice of the current function, we have explored the plane (H_c, Ω) by computing around $14 \times 14 = 196$ models, with and without electromagnetic field. We present in this section the results concerning the effect of the electromagnetic field in the (H_c, Ω) space for the particular case of the Pol2 EOS and the form (33) of the current function, the constant f_0 being adjusted in

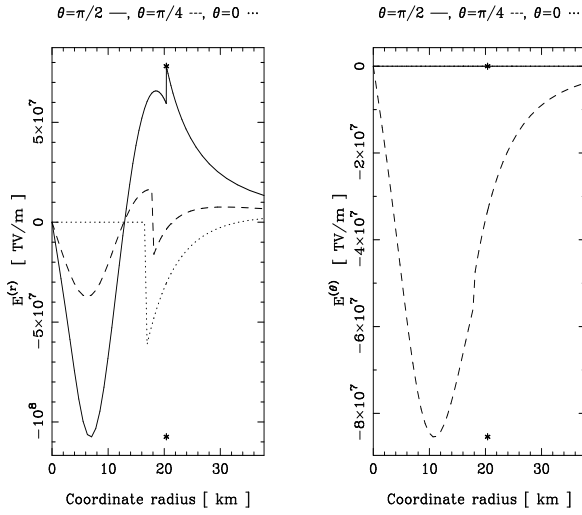


Fig. 16. Components $E_{(r)}$ (left) and $E_{(\theta)}$ (right) of the electric field corresponding to the configuration of Figs. 14 and 15. The notations are the same as in Fig. 10. On the right-hand figure, the dotted line is merged with the solid one.

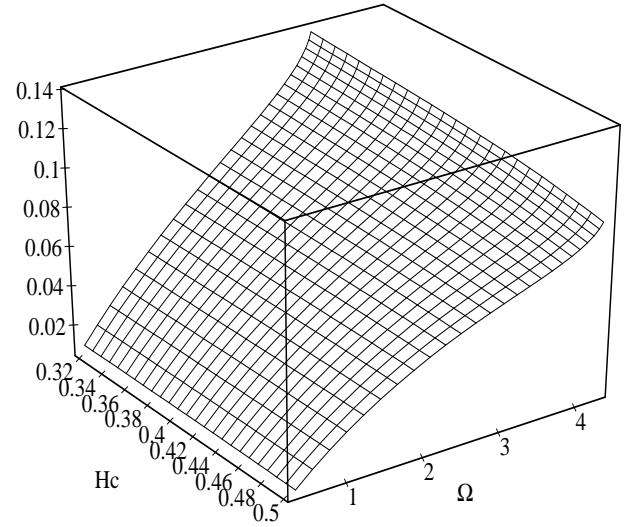


Fig. 18. Same as Fig. 17 but for the total angular momentum J [in $M_{\odot} c \text{ km}$].

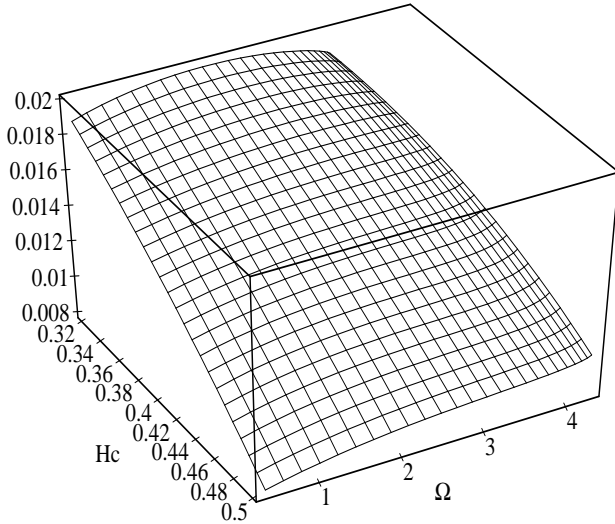


Fig. 17. Difference between the baryonic mass [in M_{\odot}] of configurations with a magnetic dipole moment $\mathcal{M} = 1.5 \cdot 10^{32} \text{ A m}^2$ and the baryonic mass of configurations without magnetic field, as a function of the central log-enthalpy H_c and the angular velocity Ω [in 10^3 rad s^{-1}], for the Pol2 EOS.

each model in order to lead to the same magnetic dipole moment $\mathcal{M} = 1.5 \cdot 10^{32} \text{ A m}^2$, so that the magnetized configurations may be considered as equivalent from a magnetic point of view for an observer sufficiently far from the star.

A first effect of the magnetic field is shown on Fig. 17: it increases the baryonic number at fixed H_c and Ω . This means that Lorentz forces, thanks to their centrifugal effect (cf. Sect. 4.1), help the star to support more baryons

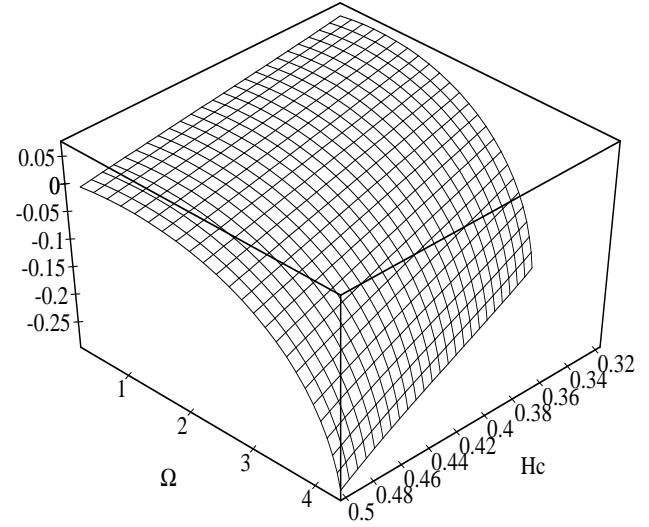


Fig. 19. Same as Fig. 17 but for the equatorial circumferential radius R_{circ} [in km].

at the same central density and same rotation rate. It appears on Fig. 17 that this effect is rather insensitive to Ω , reflecting that this is the magnetic field which contributes the most to the Lorentz force, not the electric field. It can be verified that, as in the static case, the centrifugal effect of Lorentz forces enhances the oblateness of the star.

A second effect of the magnetic field is to increase the total angular momentum J , as shown in Fig. 18, more or less linearly with respect to Ω . This augmentation is rather significative and can reach more than 1.5% of the zero magnetic field value. The redistribution of baryons inside the star induced by Lorentz forces is responsible for

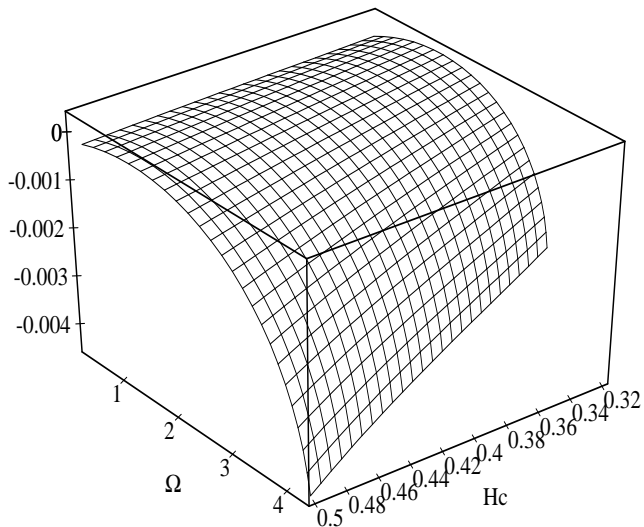


Fig. 20. Same as Fig. 17 but for the equatorial fluid velocity as measured by the locally non-rotating observer, U_{eq} [in units of c].

most of the increase, well before the contribution to J of the electromagnetic field intrinsic angular momentum.

The variation of the star's equatorial radius R_{circ} (defined as the star's equatorial circumference as measured by the observer \mathcal{O}_0 divided by 2π) is depicted in Fig. 19. For small angular velocities, the radius increases, in the continuation of the static case where it has been seen that Lorentz forces stretch the star out (Sect. 4.1). But for larger angular velocities the radius decreases instead. This may be explained in the following way. At large rotation rates the stellar equilibrium is governed by the inertial centrifugal forces. Now these forces increase with the radius and are rather important at the periphery of the star. On the contrary, the Lorentz forces are important near the centre and support there the massive nucleus of the star, so that for the same central density and rotation rate, the star can have a smaller radius to maintain the equilibrium, which is energetically favorable in so far as the peripheric inertial forces are near the shedding limit, contrary to the low rotation velocity case. Due to this reduction of the star's radius, the equatorial fluid velocity as measured by the observer \mathcal{O}_0 decrease, as it can be verified on Fig. 20.

5.4. Effect on M_{max} and Ω_{max}

Table 2 gives (i) maximum mass rotating configurations without any magnetic field (first line), (ii) along a sequence of constant magnetic dipole moment \mathcal{M} (second line) and (iii) rotating configurations with magnetic fields close to the maximum value (third line), for the EOS Pol2, PandN and BJI.

As in the static case, the maximum gravitational mass along sequences at fixed \mathcal{M} , M_{max} , increases with \mathcal{M} (cf. Figs. 21 and 23). A difference with the static case is that

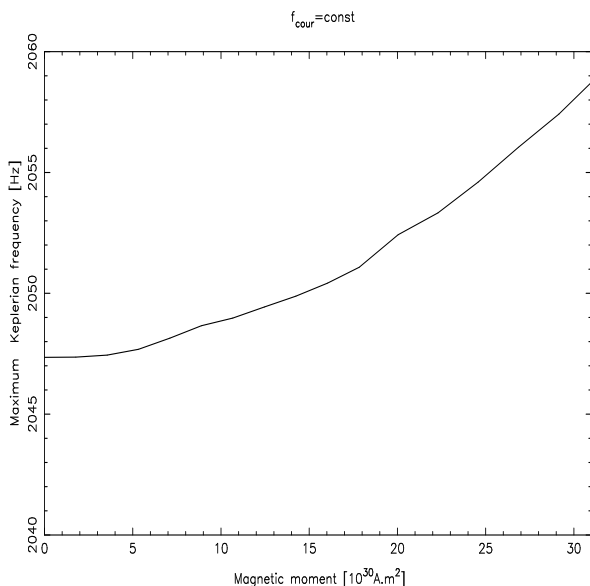


Fig. 22. Maximum Keplerian frequency $\Omega_K/2\pi$ along rotating sequences at fixed magnetic dipole moment as a function of the magnetic dipole moment for the PandN EOS.

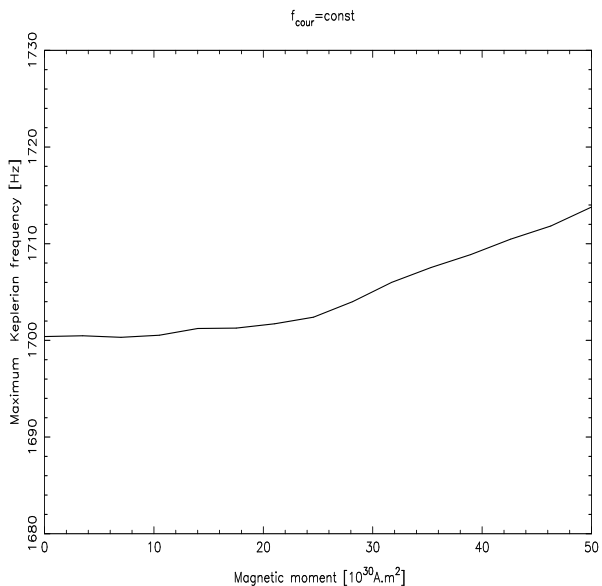


Fig. 24. Same as Fig. 22 but for the BJI EOS.

the maximum baryon number is an increasing function of \mathcal{M} for all EOS, including BJI (compare Figs. 9 and 23).

For a given central-enthalpy and magnetic dipole moment, the Keplerian angular velocity Ω_K is the value of Ω above which no stationary solution exists, the star being at the break up limit under the effect of centrifugal inertial forces. The maximum Keplerian velocity along a sequence at fixed \mathcal{M} is reached at, or very close to, the

Table 2. Neutron star configurations in the rotating case. For each EOS, the first two lines are maximum mass configurations at fixed \mathcal{M} . Ω is the angular velocity; for the first two lines of each EOS Ω is the Keplerian velocity Ω_K . $P = 2\pi/\Omega$ is the rotation period, R_{circ} the equatorial circumferential radius, J the angular momentum, Q the quadrupole moment as defined in Salgado et al. 1994a, U_{eq} the fluid velocity at the equator as measured by a locally non-rotating observer and N_c^ϕ the “dragging of the inertial frames” at the star’s centre. The remaining symbols are defined in the caption of Table 1. We use $G = 6.6726 \cdot 10^{-11} \text{ m}^3\text{kg}^{-1}\text{s}^{-2}$, $c = 2.997925 \cdot 10^8 \text{ m s}^{-1}$ and $1 M_\odot = 1.989 \cdot 10^{30} \text{ kg}$.

EOS	\mathcal{M} [10^{32} A m^2]	B_c [10^3 GT]	B_{pole} [10^3 GT]	H_c	e_c [$\rho_{\text{nuc}} c^2$]	$\frac{p_{\text{mg},c}}{p_{\text{fl},c}}$	Ω [10^4 s^{-1}]	P [ms]	M [M_\odot]	\mathcal{B} [M_\odot]	E_{bind} [$m_{\text{B}} c^2$]
Pol2	0	0	0	0.432	3.43	0	0.398	1.58	3.63	3.99	-0.0897
	1.95	22.6	5.42	0.432	3.43	0.02	0.404	1.56	3.68	4.04	-0.0880
	3.98	41.9	11.3	0.400	3.06	0.08	0.389	1.62	3.76	4.11	-0.0852
PandN	0	0	0	0.668	21.7	0	1.29	0.488	1.93	2.23	-0.1313
	0.24	54.6	15.2	0.664	21.5	0.01	1.29	0.487	1.94	2.23	-0.1297
	1.07	251.9	88.7	0.600	19.1	0.23	1.16	0.543	1.97	2.20	-0.1071
BJI	0	0	0	0.628	16.3	0	1.07	0.588	2.15	2.46	-0.1240
	0.50	68.0	19.0	0.619	16.0	0.02	1.08	0.584	2.18	2.48	-0.1207
	1.45	172.5	60.2	0.500	12.5	0.21	0.896	0.701	2.19	2.45	-0.1066

EOS	R_{circ} [km]	$\frac{cJ}{GM^2}$	$\frac{Q}{MR_{\text{circ}}^2}$	$\frac{U_{\text{eq}}}{c}$	$\frac{N_c^\phi}{\Omega}$	GRV2	GRV3
Pol2	31.0	0.570	0.0239	0.468	0.648	6E-06	1E-05
	31.1	0.580	0.0256	0.475	0.657	9E-03	1E-03
	29.3	0.589	0.0344	0.427	0.658	4E-03	4E-04
PandN	11.4	0.641	0.0320	0.576	0.805	1E-04	7E-05
	11.4	0.646	0.0325	0.579	0.807	7E-03	6E-04
	9.9	0.593	0.0444	0.431	0.833	6E-03	7E-04
BJI	13.4	0.626	0.0298	0.559	0.784	4E-05	9E-05
	13.4	0.638	0.0318	0.566	0.789	5E-03	4E-04
	12.1	0.575	0.0433	0.407	0.780	5E-03	3E-04

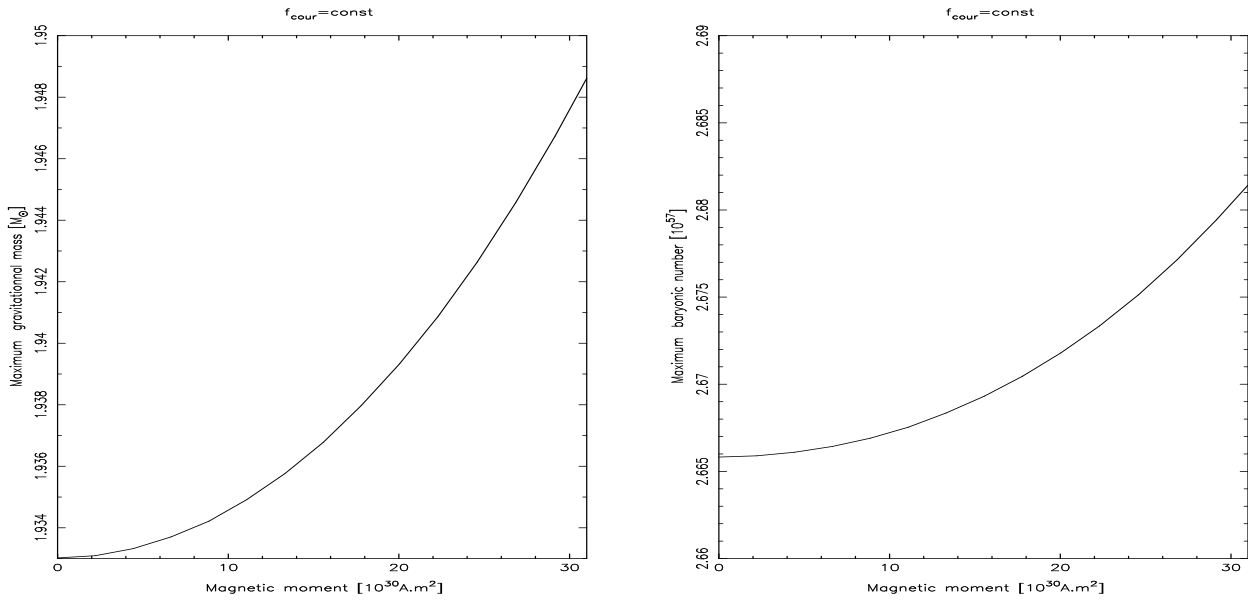


Fig. 21. Maximum gravitational mass (left) and maximum baryon number (right) along rotating sequences at fixed magnetic dipole moment as a function of the magnetic dipole moment for the PandN EOS.

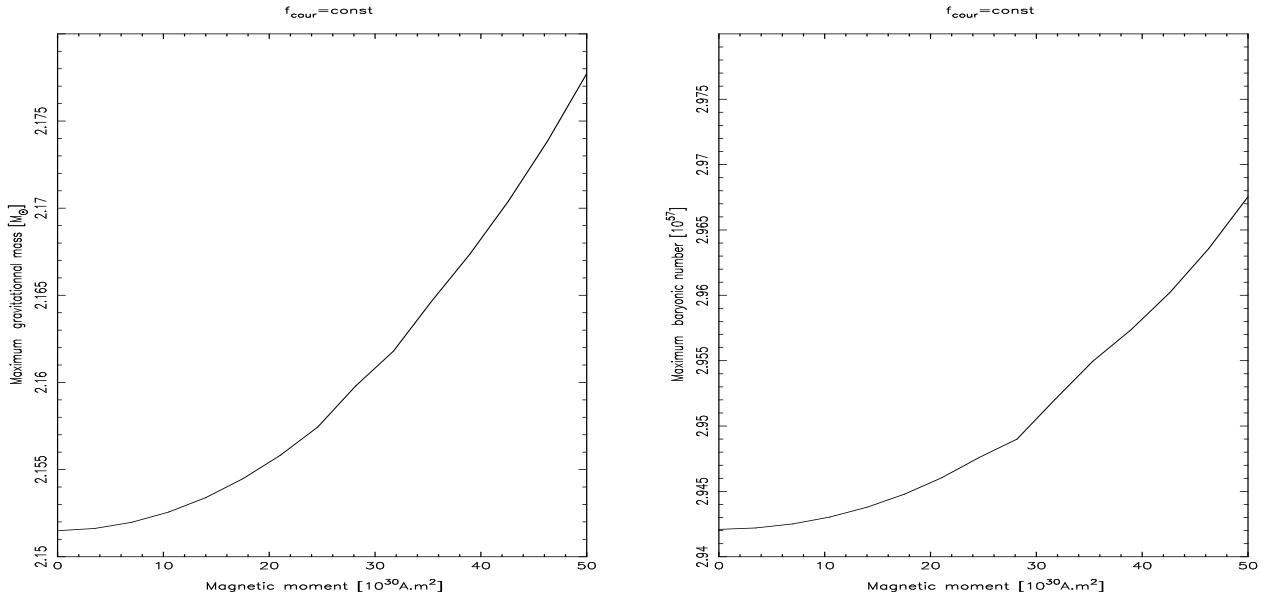


Fig. 23. Same as Fig. 21 but for the BJI EOS.

maximum mass configuration. As seen from Figs. 22 and 24, the maximum Ω_K increases with \mathcal{M} .

6. Magnetized sequences at constant baryon number

Constant baryon number sequences may represent the time evolution of a neutron star and have been investigated in recent studies of non-magnetized rotating neutron stars (Cook et al. 1994b, Salgado et al. 1994a,b).

We analyze in this section the behaviour of constant baryon number sequences at a fixed magnetic dipole moment $\mathcal{M} = 1.5 \cdot 10^{32} \text{ A m}^2$, by stressing the differences with the non-magnetized case.

6.1. Normal sequence

A *normal* sequence is a sequence with a baryon number lower than the maximum one supported by non-rotating configurations. We consider a sequence at baryonic mass $\mathcal{B} = 3.00 M_\odot$, built with the Pol2 EOS and the choice (33) for the current function f . Let us first mention that the choice $\mathcal{M} = 1.5 \cdot 10^{32} \text{ A m}^2$ corresponds to highly magnetized objects, the polar value of the magnetic field varying from $B = 1.4 \cdot 10^3 \text{ GT}$ ($\Omega = 0$) to $B = 5.0 \cdot 10^2 \text{ GT}$ ($\Omega = \Omega_K$) along the sequence. The difference between various characteristic quantities of magnetized and non-magnetized stars of the sequence are represented in Fig. 25. According to Fig. 25a the magnetic field increases the gravitational mass, but only by a small amount (for the chosen value of \mathcal{M}), around one thousandth. The angular momentum increase is more substantial, being of the order of 3% (Fig. 25b). The star's radius

increases under the centrifugal effect of the Lorentz forces by roughly 5% (Fig. 25c) and consequently the central energy density decreases, by roughly 4% (Fig. 25c). For this normal sequence, the response of the global quantities to the magnetic field is the same as in the static case (cf Sect. 4).

We have also constructed normal sequences with the PandN EOS. Their behaviour is very similar to that described above.

6.2. Supramassive sequence

A *supramassive* sequence is a sequence with a baryon number in excess of the maximum value that can be supported in the absence of rotation. We consider a supramassive sequence which in addition presents the phenomenon of *spin-up by angular momentum loss* (Cook et al. 1994a): the $\mathcal{B} = 3.80 M_\odot$ sequence built on the Pol2 EOS. The fact that along this sequence a decrease of angular momentum leads to an increase of angular velocity is demonstrated in Fig. 7 of Salgado et al. (1994a). The sequence begins at the angular velocity $\Omega = 3.20 \cdot 10^3 \text{ rad s}^{-1}$ and ends at the stability limit $\Omega = 3.52 \cdot 10^3 \text{ rad s}^{-1}$. The electromagnetic effects are reported in Fig. 26 and appear to differ from those of the normal sequence. The gravitational mass decreases for the lowest angular velocities and increases for the highest ones (Fig. 26a), whereas the angular momentum decreases all the time (Fig. 26b). This decrease in angular momentum can be attributed mainly to the star's radius decrease (Fig. 26c). This latter behaviour contrasts with the normal sequence case (cf. Fig. 25c) and can be explained as follows. Near the minimum angular velocity ($\Omega = 3.20 \cdot 10^3 \text{ rad s}^{-1}$), the centrifugal forces take their

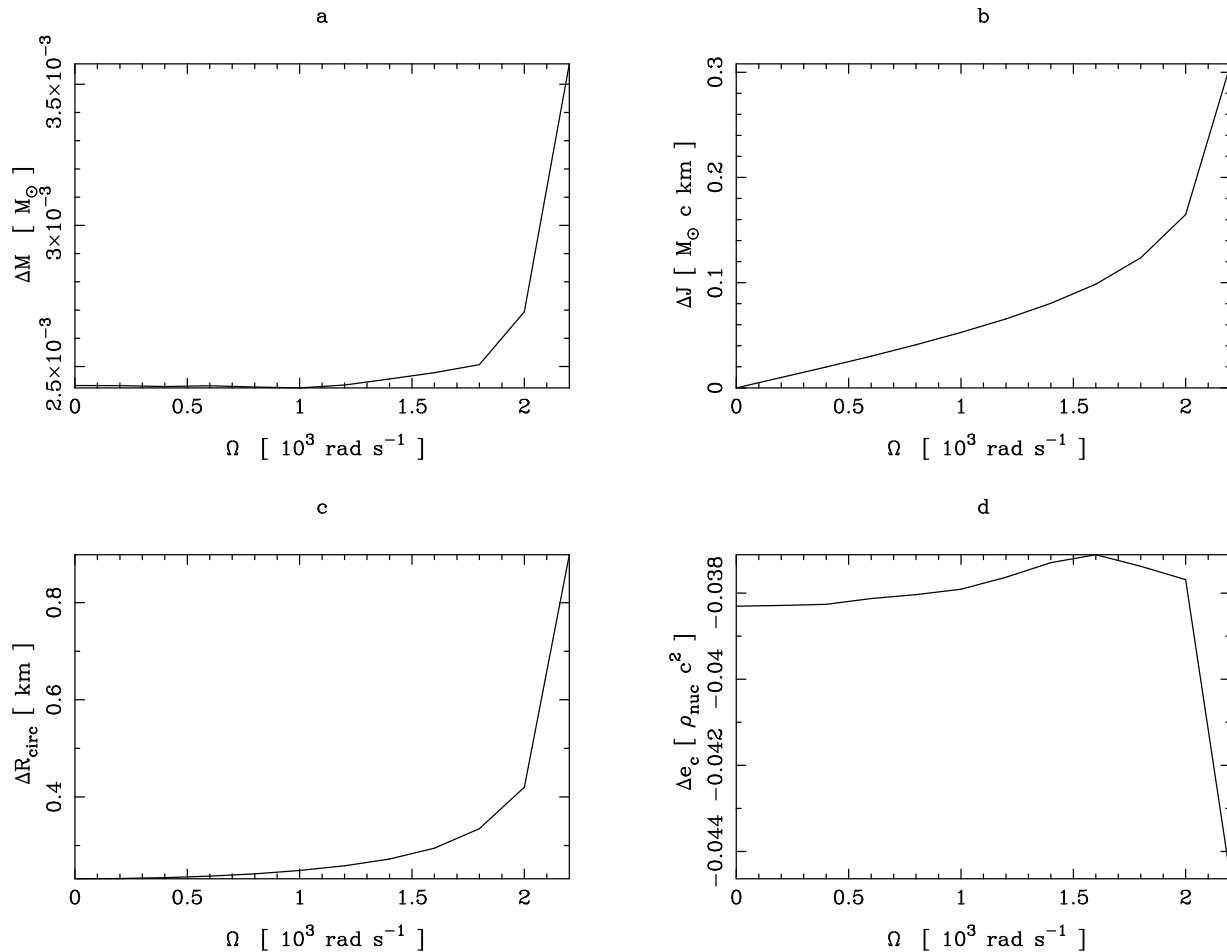


Fig. 25. Differences between configurations without magnetic field and with a magnetic dipole moment $\mathcal{M} = 1.5 \cdot 10^{32} \text{ A m}^2$ along a sequence at constant baryonic mass $\mathcal{B} = 3.00 M_\odot$ for the Pol2 EOS and the current function $f(x) = \text{const}$: (a) gravitational mass difference ΔM ; (b) angular momentum difference ΔJ ; (c) circumferential radius difference ΔR_{circ} ; (d) central energy density difference Δe_c . The path along the sequence is parametrized by the angular velocity Ω .

origin, not in a high rotation rate, but in a large spatial extension. The Lorentz forces play then a greater role in the equilibrium of the star since they are mainly localised in the star's centre and are more efficient in supporting the star than the centrifugal forces, which are localised at the star's periphery. The replacement of the centrifugal forces by the Lorentz ones in balancing gravity leads to a smaller stellar radius. This can be illustrated by the following example: a star (built upon the Pol2 EOS) of baryon mass $3.77 M_\odot$ and central density $3.1 \rho_{\text{nuc}}$ has a circumferential radius of 26.5 km if it is supported by rotation ($\Omega = 3.3 \times 10^3 \text{ rad s}^{-1}$) and only 21.2 km if it is static and supported by the magnetic field ($\mathcal{M} = 7.02 \times 10^{32} \text{ A m}^2$), for the same number of baryons. This phenomenon explains the negative value of ΔR_{circ} in Fig. 26c which reaches -9% at $\Omega = 3.20 \cdot 10^3 \text{ rad s}^{-1}$. When Ω increases the centrifugal forces become more efficient and the decrease of the star's radius with respect to

the non-magnetized case becomes less pronounced. Due to the contraction of the star, the central density increases (Fig. 26d). According to this explanation, the same phenomenon should exist in the Newtonian case, but we have not conducted a systematic study of Newtonian configurations.

7. Conclusion

We have extended an existing numerical code for computing perfect fluid rotating neutron stars in general relativity (BGSM, Salgado et al. 1994a,b) to include the electromagnetic field. This latter is calculated by solving the relativistic Maxwell equations with an electric current distribution which is compatible with the star's equilibrium (i.e. the Lorentz force acting on the conducting fluid shall be the gradient of some scalar in order to balance gravity and the inertial centrifugal force). In order to preserve the sta-

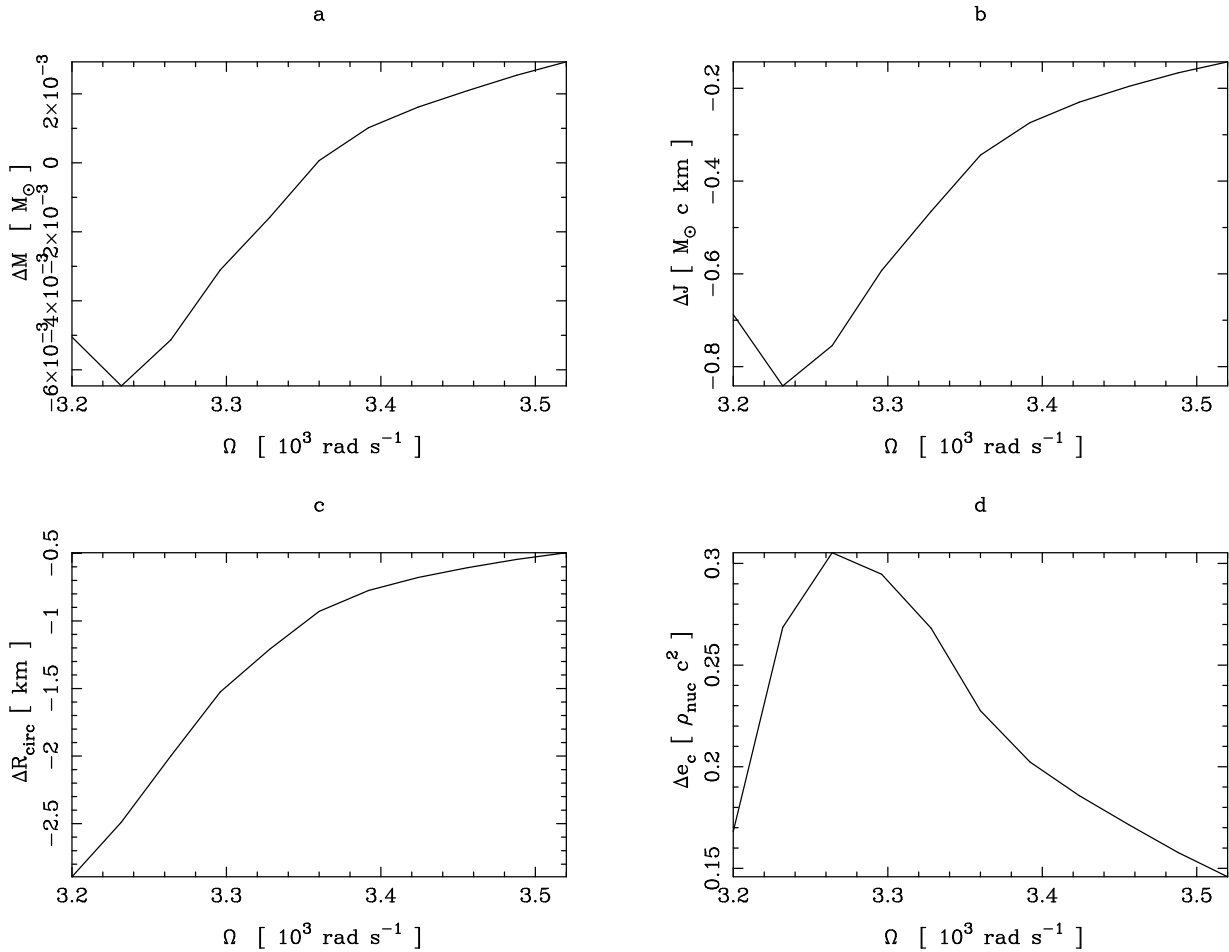


Fig. 26. Same as Fig. 25 but for a supramassive sequence at $B = 3.80 M_{\odot}$.

tionarity, axisymmetry and circularity properties of space-time, we consider only axisymmetric poloidal magnetic fields. The equations are numerically solved by means of a pseudo-spectral technique which results in a high accuracy as tests on simple electromagnetic configurations (for which an analytical solution is available) have shown: the relative error on the electromagnetic field is of the order of 10^{-5} inside the star and 10^{-9} outside it. The part of the code relative to the deformation of the star by Lorentz forces has been tested by comparison with Ferraro’s analytical solution in the Newtonian case. The fact that the numerical output is a solution of Einstein equations has been tested by two virial identities: GRV2 and GRV3.

We have then used the code to investigate the effect of the magnetic field on rotating neutron stars. For this purpose we considered magnetic field amplitude ranging from zero up to huge values, of the order of 10^5 GT, which is ten thousand times bigger than the highest measured values at the pulsars surfaces and is the value for which the magnetic pressure equals (with an opposite sign along the symmetry axis) the fluid pressure near the centre of the

star. Let us note that such enormous magnetic fields are expected to decay on very short time scales via the mechanism of ambipolar diffusion, as investigated by Haensel et al. (1991), Goldreich & Reisenegger (1992) and Urpin & Shalybkov (1995), which is very efficient when the electric current is perpendicular to \mathbf{B} , as in the present case. The decay time scale for non-superconducting matter computed by the above authors is 10^2 yr for $B \sim 10^4$ GT and 10^6 yr for $B \sim 1$ GT.

According to our study, the influence of the magnetic field on the star’s structure is mostly due to Lorentz forces and not to the gravitational field generated by the electromagnetic stress-energy. This may be understood once it has been realized that a magnetic field of 10^5 GT has an energy density of $0.25 \rho_{\text{nuc}} c^2$, whereas the matter density at the centre of neutron stars is between 1 and $10 \rho_{\text{nuc}}$. Although the electromagnetic energy is much lower than the fluid mass-energy, the deformation of the star can be as dramatic as that of Fig. 5 because of the *anisotropic* character of the magnetic pressure, just as the anisotropic centrifugal forces can highly deform the star in the rotat-

ing case though the kinetic energy is much lower than the fluid rest mass.

In static and slowly rotating cases, Lorentz forces stretch the star away from the symmetry axis. The deformation is appreciable only for $B > 10^2$ GT. In highly relativistic situations (supramassive sequences), the effect of the magnetic field is instead to reduce the star's equatorial radius (at fixed baryon number).

The maximum poloidal magnetic field supported by neutron stars has a polar value between 4×10^4 and 1.5×10^5 GT depending upon the EOS and the rotation state of the star. Let us recall that the magnetic field at the star's centre is two to four times higher than at the poles.

The impact of the magnetic field on the maximum mass of neutron stars is very limited for magnetic fields of the order of 1 GT, whereas it is important for the magnetic fields near the maximum value ($\sim 10^5$ GT): in the static case, M_{\max} is increased by 13% to 29% — depending upon the EOS — with respect to non-magnetized configurations. In fact, the magnetic field reveals to be more efficient in increasing M_{\max} than the rotation, except for the EOS HKP, where the maximum mass in rotation (without any magnetic field) is 21.2% higher than M_{\max} for stationary configurations (Salgado et al. 1994a), whereas the static magnetized M_{\max} is only 13.3% higher. For the PandN EOS, the M_{\max} increase by both mechanisms are similar ($\sim 16\%$), whereas for the Pol2, BJI and Diaz II EOS, the static magnetized M_{\max} lies above the rotating non-magnetized M_{\max} .

In the future, we plan to study the stability of the magnetized configurations presented in this article. Two types of instabilities may be expected to occur for high values of B : (i) a pure electromagnetic instability towards another electric current - magnetic field distribution (of lower energy) and (ii) a non-axisymmetric instability resulting in a triaxial stellar equilibrium shape, which would be the magnetic analog of the transition from the MacLaurin spheroids to the tri-axial Jacobi ellipsoids for high rotational velocities of Newtonian incompressible bodies.

Acknowledgements. We thank Pawel Haensel for his careful reading of the manuscript and many remarks about the physics of the magnetic field in neutron star interiors. We are grateful to the anonymous referee for useful comments that helped us to improve the paper. The numerical computations have been performed on Silicon Graphics workstations purchased thanks to the support of the SPM department of the CNRS and the Institut National des Sciences de l'Univers.

References

Bardeen J.M., 1970, ApJ 162, 71
 Bardeen J.M., 1973, in: DeWitt C., DeWitt B.S. (eds.) Black Holes — Les Houches 1972, Gordon and Breach, New York, p. 241
 Bethe H.A., Johnson M.B., 1974, Nucl. Phys. A 230, 1
 Bonazzola S., Gourgoulhon E., 1994, Class. Quantum Grav. 11, 1775

Bonazzola S., Gourgoulhon E., Salgado M., Marck J.A., 1993, A&A 278, 421 (referred to in the text as BGSM)
 Bonazzola S., Marck J.A., 1990, J. Comp. Phys. 87, 201
 Carter B., 1973, in: DeWitt C., DeWitt B.S. (eds.) Black Holes — Les Houches 1972, Gordon and Breach, New York, p. 125
 de Castro A., 1991, Am. J. Phys. 59, 180
 Chandrasekhar S., Fermi E., 1953, ApJ 118, 116
 Cohen J.M., Kegeles L.S., Rosenblum A., 1975, ApJ 201, 783
 Cook G.B., Shapiro S.L., Teukolsky S.A., 1994a, ApJ 422, 227
 Cook G.B., Shapiro S.L., Teukolsky S.A., 1994b, ApJ 424, 823
 Diaz Alonso J., 1985, Phys. Rev. D31, 1315
 Eriguchi Y., Hachisu I, Nomoto K, 1994, MNRAS 266, 179
 Ferraro V.C.A., 1954, ApJ 119, 407
 Feynman R.P., Leighton R.B., Sands M., 1964, The Feynman Lectures on Physics. Addison-Wesley, Reading, vol. 2, p. 17-5
 Friedman J.L, Ipser J.R., 1992, Phil. Trans. R. Lond. A 340, 391, reprinted in: Chandrasekhar S. (ed.) Classical General Relativity. Oxford University Press, Oxford (1993)
 Goldreich P., Reisenegger A., 1992, ApJ 395, 250
 Gourgoulhon E., Bonazzola S., 1993, Phys. Rev. D 48, 2635
 Gourgoulhon E., Bonazzola S., 1994, Class. Quantum Grav. 11, 443
 Haensel P., Kutschera M., Proszynski, 1981, A&A 102, 299
 Haensel P., Urpin V.A., Yakovlev D.G., 1991, A&A 229, 133
 Ma T.-C. E., 1986, Am. J. Phys. 54, 949
 Michel F.C., 1991, Theory of neutron star magnetospheres. University of Chicago Press, Chicago
 Pandharipande V.R., 1971, Nucl. Phys. A 174, 641
 Ruffini R., Treves A., 1973, Astrophysical Letters 13, 109
 Sakurai T., 1985, A&A 152, 121
 Salgado M., Bonazzola S., Gourgoulhon E., Haensel P., 1994a, A&A 291, 155
 Salgado M., Bonazzola S., Gourgoulhon E., Haensel P., 1994b, A&AS 108, 455
 Sauty C., Tsinganos K., 1994, A&A 287, 893
 Smarr L., York J. W., 1978, Phys. Rev. D 17, 2529
 Taylor J.H., Manchester R.N., Lyne A.G., 1993, ApJS 88, 529
 Thompson C., Duncan R.C., 1993, ApJ 408, 194
 Thorne K.S., Price R.H., Macdonald D.A. (eds.), 1986, Black Holes: The Membrane Paradigm. Yale University Press, New Haven
 Urpin V.A., Ray A., 1994, MNRAS 267, 1000
 Urpin V.A., Shalybkov D.A., 1995, A&A 294, 117
 Wiebicke H.-J., Geppert U., 1995, A&A 294, 303

This article was processed by the author using Springer-Verlag L^AT_EX A&A style file L-AA version 3.